INTERNATIONAL JOURNAL FOR NUMERICAL METHODS IN ENGINEERING
Int. J. Numer. Meth. Engng 2007; **72**:549–581
Published online 5 March 2007 in Wiley InterScience (www.interscience.wiley.com). DOI: 10.1002/nme.2020

Embedded strong discontinuity finite elements for fractured geomaterials with variable friction

C. D. Foster[1], R. I. Borja[1,*,†] and R. A. Regueiro[2]

[1]*Civil and Environmental Engineering, Stanford University, Stanford, CA 94305-4020, U.S.A.*
[2]*Civil, Environmental, and Architectural Engineering, Engineering Center ECOT 441, University of Colorado, Boulder, UCB 428, Boulder, CO 80309, U.S.A.*

SUMMARY

The strong discontinuity approach to modelling strain localization, combined with an enhanced strain element, has been used for more than a decade to model strain localization in materials including geomaterials. Most implementations of enhanced strain elements in the post-localization regime use very simple constitutive formulations along the discontinuity, such as linear softening or a constant friction coefficient. However, the softening relations can be much more complex for geomaterials. For rocks this softening is induced by micro-fractures coalescing into macroscopic cracks during a narrow time interval called 'slip weakening.' During this interval the cohesive resistance on the nucleating crack decays to zero while the frictional resistance increases. Furthermore, research has shown that the coefficient of friction for these materials is not constant, but in fact is a function both of the slip speed and the state of the material, including wear, temperature, and other factors. In this paper we augment the modelling capabilities of an enhanced strain element by incorporating a cohesive softening law and a popular rate- and state-dependent friction model commonly used for describing the constitutive properties of rocks and rock-like materials sliding along the fractured surface. Copyright © 2007 John Wiley & Sons, Ltd.

Received 23 April 2006; Revised 11 January 2007; Accepted 15 January 2007

KEY WORDS: bifurcation; rate- and state-friction; strong discontinuity; enhanced strain; finite element

1. INTRODUCTION

Strain localization, characterized by intense deformation across a narrow region, plays an important role in the behaviour of many solid materials. Examples include shear banding and necking in

*Correspondence to: R. I. Borja, Civil and Environmental Engineering, Stanford University, Stanford, CA 94305-4020, U.S.A.
†E-mail: borja@stanford.edu

Contract/grant sponsor: U.S. Department of Energy; contract/grant number: DE-FG02-03ER15454
Contract/grant sponsor: U.S. National Science Foundation; contract/grant number: CMG-0417521

metals, necking in polymers, and shear fracturing in bulk metallic glasses. In geomaterials we observe shear, compaction, and dilation bands in porous rocks; shear and tensile fractures in more brittle rocks, ceramics, and concrete; shear bands in sands, and cracking in heavily overconsolidated clays. In addition to potentially significant displacements, an associated rapid loss of strength makes strain localization an important area of study, as this loss of strength can lead to structural failure or other unstable behaviours.

Traditional geotechnical analyses of localized deformation are typically conducted by limit equilibrium methods such as those based on the method of slices for the analysis of slope stability. These methods assume to some degree the shape of the failure surface, and, since they are based on statics, give no information on elastic or plastic deformations before or after localization. Another limitation of the limit equilibrium methods is that they impart no information on the post-localization state of the structures being analysed. These methods do seem to provide reasonable, if conservative, results for standard geotechnical engineering problems such as slope stability analysis. However, for more complex geometries the predictive capabilities of these methods are likely inadequate.

An alternative is to employ a numerical technique, such as the finite element method, to capture the localization. However, while standard finite element methods have proven useful for a wide variety of geometries, loading, and deformation patterns, modelling localized deformation using standard elements is difficult and can lead to inaccurate results. Classical associative and non-associative plasticity models could lead to non-unique strain rate fields [1, 2], requiring a special treatment of the local bifurcation and accompanying strain localization. Where the path of the localization is easily predicted, such as along a weak interface between two existing rock layers, the mesh can be aligned with along the discontinuity, and contact elements [3, 4], cohesive surface elements [5, 6], or similar techniques may be employed.

In general, however, the location and propagation direction of the localized region may not be known *a priori*, and can greatly influence the response. A variety of methods have been developed to attempt to capture localization in this case. One broad class of techniques involves adding additional information to governing equations to keep their character constant. These techniques include viscous regularization [7, 8], non-local [9, 10] and gradient plasticity [11–13], and micropolar (Cosserat) continua [14, 15]. All of these techniques can regularize the solution, but require additional parameters to be determined. While some of these techniques were developed primarily to regularize the equations, much recent work has linked these parameters to physically based phenomena such as grain size. As the bands develop naturally from the governing equations, these techniques hold significant promise for modelling the deformation bands. A major drawback of these methods, however, is that they require several elements across the thickness of the band to accurately resolve the deformation. When the location of the localized region is not initially known, this requirement can result in meshes too fine to be computationally tractable. The expense may be particularly acute in geotechnical and geological problems where the difference in length scales between the localized region (millimeters to centimeters) and the problem of interest (meters or kilometers) is several orders of magnitude.

To this end a second set of techniques has been developed that incorporate a deformation band within an element. These methods model the band with either a jump in the strain field, termed a ‘weak discontinuity’, or in the displacement field, a ‘strong discontinuity’. Weak discontinuity methods include [16–18]. Many deformation bands have finite width, including shear bands in soils, and even fractures in concrete and many rocks have fracture process zone that leave a finite width of gouge material. To avoid spurious mesh dependency, these methods must include a length

DOI: 10.1002/nme

scale, the width of the band, which does not come from the governing equations and must be determined as an additional material parameter.

In contrast, strong discontinuity methods [16, 19–48], while giving up some physical significance of the band width, do not require a length scale (or more properly set that length scale to zero). The two methods are quite closely related, and if the element size is significantly larger than the band width, behave very similarly. Formulations of both methods allow for the insertion of the band at arbitrary orientation and locations within the element, tracking of the band continuously across a mesh, and condensation of the extra degree of freedom at the element level. Armero [19] demonstrated that weak discontinuity response may be approximated by a strong discontinuity formulation, provided that the dissipation across the band is properly captured. Oliver and coworkers [49] formulated a model that proceeds from intact continuum to weak discontinuity, to strong discontinuity.

The formulation in this paper follows the strong discontinuity formulation of Simo and co-workers [20, 21], and more closely the reformulation of Borja and Regueiro [33–38], which is described in more detail in Section 3. Other sub-classes of this element type have been described and differ primarily in the way the extra degrees of freedom are condensed; see [30, 39] for reviews of the various types of these elements. The amount of slip along the surface is determined by a surface constitutive law. The main body of this paper is dedicated to the numerical formulation and implementation of this constitutive response into the enhanced strain element. We will discuss both a generic implementation, and a specific implementation for a combined slip weakening and frictional response applicable to rocks and rock-like materials.

For geomaterials and other quasi-brittle materials undergoing strain localization, the constitutive behaviour can be approximately broken into two phases. The first phase is slip weakening, where the cohesive strength of the material degrades as a coherent macrocrack forms. During slip weakening a frictional response along the surface of discontinuity also develops. The coefficient of friction has been shown to vary with slip speed and state of the material, including factors such as wear, gouge material between the surfaces, and temperature. To capture this behaviour, we use a rate- and state-dependent friction model developed by Ruina, Dieterich, and Rice, among others [50–52].

The main contribution of this paper is the incorporation of a variable coefficient of friction into the strong discontinuity formulation. A variable coefficient of friction is atypical in computational mechanics literature where a constant coefficient of friction is almost always assumed. However, it is widely recognized in geophysics and in many branches of geoscience that the coefficient of friction may depend not only on slip speed but also on a state parameter representing the maturity of contact. Thus, it cannot be assumed to be constant for important applications such as earthquake fault rupture processes. In this paper we focus on a velocity- and state-dependent coefficient of friction applicable to slow slip velocities and laboratory-derived state and friction laws, along with the strong discontinuity finite element formulation.

The remainder of the paper is structured as follows: we briefly review in Section 2 the kinematical assumptions for a strong discontinuity in the context of small strain deformation and the resulting bifurcation condition. Then we present in Section 3 the proposed framework for enhanced strain element and its implementation. Section 4 discusses the constitutive laws, the friction model, and the slip weakening algorithm (which may be coupled with a general friction law). We present the numerical formulation for determining the slip in Section 5, and the resulting consistent stiffness formulation in Section 6. Numerical examples and concluding remarks close out the paper.

DOI: 10.1002/nme

2. KINEMATICS

As a point of departure, we examine kinematics that include a strong discontinuity. For the purposes of this paper, we will use small strain assumptions. Strong discontinuity kinematics in a finite deformation setting are described in more detail in [22, 38].

Consider a body with an otherwise smooth displacement field that contains a displacement jump across the surface S in the body. In other words

$$\begin{aligned}\mathbf{u} &= \bar{\mathbf{u}} + [\![\mathbf{u}]\!] H_S \\ &= \bar{\mathbf{u}} + \zeta \mathbf{m} H_S \end{aligned} \tag{1}$$

where H_S is a Heaviside function across S. The vector $\bar{\mathbf{u}}$ is referred to as the regular part of the displacement, while $[\![\mathbf{u}]\!]$ is the displacement jump. The magnitude of the jump is ζ, in the direction $\mathbf{m}$. In granular materials, dilation on cracks is observed due to asperity mismatch and the formation of gouge material, and has been shown to have important impacts on crack behaviour [53]. Hence, the slip direction is expected to not be exactly perpendicular to the normal to the slip surface. As slip continues, however, there is less further dilation, and $\mathbf{m}$ becomes closer to being parallel to the band.

In the infinitesimal regime, the strain field becomes

$$\boldsymbol{\varepsilon} = \nabla^{\mathrm{s}} \mathbf{u} = \nabla^{\mathrm{s}} \bar{\mathbf{u}} + \nabla^{\mathrm{s}} (\zeta \mathbf{m}) H_S + \zeta (\mathbf{m} \otimes \mathbf{n})^{\mathrm{s}} \delta_S \tag{2}$$

with $\mathbf{n}$ as the normal to S, δ_S the Dirac delta distribution across S, and $(\bullet)^{\mathrm{s}}$ denoting the symmetric part of the tensor $(\bullet)$. The spatial gradient of the jump will generally be quite small compared to the jump itself. In the finite element approximation, we consider the jumps to be constant within a given element, so the second term disappears, leaving

$$\boldsymbol{\varepsilon} = \nabla^{\mathrm{s}} \mathbf{u} = \nabla^{\mathrm{s}} \bar{\mathbf{u}} + \zeta (\mathbf{m} \otimes \mathbf{n})^{\mathrm{s}} \delta_S \tag{3}$$

For the finite element formulation, it is convenient to reformulate the displacement field as

$$\begin{aligned}\mathbf{u} &= \tilde{\mathbf{u}} + \hat{\mathbf{u}} \\ &= \tilde{\mathbf{u}} + [\![\mathbf{u}]\!] M_S \\ &= (\bar{\mathbf{u}} + f^h [\![\mathbf{u}]\!]) + [\![\mathbf{u}]\!] (H_S - f^h) \end{aligned} \tag{4}$$

Here f^h is an arbitrary smooth function that is equal to zero at all the element nodes on the 'passive' side of the element, where $H_S = 0$, and unity at all the nodes on the 'active' side, where $H_S = 1$.

We use a convenient and typical form for f^h, the sum of the shape functions of the active nodes

$$f^h = \sum_{A=1}^{n_{\mathrm{en}}} N_A H_S(\mathbf{x}_A) \tag{5}$$

where n_{en} is the number of nodes for a particular element, and N_A are the standard finite element shape functions. This form is useful because now $\tilde{\mathbf{u}}$ can be written in the standard finite

DOI: 10.1002/nme

element form

$$\tilde{\mathbf{u}}^h = \sum_{A=1}^{n_{\text{en}}} N_A \mathbf{x}_A \tag{6}$$

Thus, with this choice of f^h, the component $\tilde{\mathbf{u}}$ of the displacement is referred to as the conforming displacement, since it conforms to the standard finite element shape functions. The vector $\hat{\mathbf{u}}$ is referred to as the displacement enhancement.

2.1. Localization condition

Given the above kinematics, it is possible to derive the conditions for localization from principles of continuum mechanics.

Consider a material undergoing standard bulk plasticity, which may follow a non-associative flow rule. Without reviewing specific plasticity models, the model is described by a yield function $F = F(\boldsymbol{\sigma}, \mathbf{q})$, where $\mathbf{q}$ is a vector of internal state variables, a plastic potential function $G = G(\boldsymbol{\sigma}, \mathbf{q})$, which may be different from F, and a hardening/softening law. If $F = G$, the flow rule is associative.

To form or propagate a discontinuity on a given surface, the traction and traction rate must be continuous across that surface. The traction rate may be written

$$\begin{aligned}\dot{\mathbf{t}} &= \mathbf{n} \cdot \dot{\boldsymbol{\sigma}} = \mathbf{n} \cdot \mathbf{c}^e : \dot{\boldsymbol{\varepsilon}}^e \\ &= \mathbf{n} \cdot \mathbf{c}^e : \left(\dot{\boldsymbol{\varepsilon}} - \dot{\lambda} \frac{\partial G}{\partial \boldsymbol{\sigma}} \right) \\ &= \mathbf{n} \cdot \mathbf{c}^e : \nabla^{\text{s}} \dot{\hat{\mathbf{u}}} + \mathbf{n} \cdot \mathbf{c}^{\text{ep}} : (\llbracket \dot{\mathbf{u}} \rrbracket \otimes \mathbf{n})^{\text{s}} \delta_S \end{aligned} \tag{7}$$

where $\mathbf{c}^{\text{ep}}$ is the elastic–perfectly plastic modulus as shown in [33]. To ensure that the tractions are bounded, the quantity $\mathbf{n} \cdot \mathbf{c}^{\text{ep}} : (\llbracket \dot{\mathbf{u}} \rrbracket \otimes \mathbf{n})^{\text{s}}$ must be zero. Exploiting the minor symmetry of $\mathbf{c}^{\text{ep}}$, this condition may be rewritten as

$$\mathbf{Q} \cdot \llbracket \dot{\mathbf{u}} \rrbracket = \mathbf{0} \tag{8}$$

where $\mathbf{Q} = \mathbf{n} \cdot \mathbf{c}^{\text{ep}} \cdot \mathbf{n}$ is the elastic–perfectly plastic acoustic tensor. Hence a bifurcation of the type described by the kinematics in the previous section may occur only when

$$\det \mathbf{Q} = 0 \tag{9}$$

for some normal $\mathbf{n}$. If we let $\llbracket \dot{\mathbf{u}} \rrbracket = \dot{\zeta} \mathbf{m}$, where $\mathbf{m}$ is a unit vector in the direction of the jump, then $\mathbf{m}$ becomes the normalized zero eigenvector for $\mathbf{Q}$. Hence, the localization condition returns the direction of the jump at bifurcation. This condition is similar to the weak discontinuity (strain jump) condition formulated in [1].

Localization may occur for any normal $\mathbf{n}$. To determine a critical normal, a numerical search algorithm in three dimensions as described in [16, 46] is employed. A reduced version of the same algorithm has also been developed for two-dimensional problems. These algorithms are modified somewhat from the original form, as plasticity models for geomaterials often have non-associative or kinematically hardening components. These features destroy the major symmetry of the tangent modulus assumed in the above formulations. Fortunately, the patch is relatively simple and can be accomplished simply by symmeterizing the matrix referred to as $\mathbf{J}$ in [16].

DOI: 10.1002/nme

3. BACKGROUND ON ENHANCED STRAIN ELEMENT

The element used is adapted from [36, 37]. The reader is referred to those papers for more detailed formulation of the element. The idea is that a jump in the displacement field is allowed across the element at arbitrary location, and with a slip direction **m**, as shown in Figure 1. Some of the relevant details to our discussion are included below.

The Galerkin form of the equations with the enhanced strain field [36] may be written

$$\int_{\Omega^h} \nabla^{\mathrm{s}} \tilde{\boldsymbol{\eta}}^h : \boldsymbol{\sigma}^h \, \mathrm{d}\Omega = \int_{\Omega^h} \tilde{\boldsymbol{\eta}}^h \cdot \mathbf{b}^h \, \mathrm{d}\Omega + \int_{\Gamma_t^h} \tilde{\boldsymbol{\eta}}^h : \mathbf{t}^h \, \mathrm{d}\Gamma \tag{10}$$

$$\int_{\Omega^h_{\mathrm{loc}}} \hat{\boldsymbol{\gamma}} \cdot \boldsymbol{\sigma}^h \, \mathrm{d}\Omega = 0 \tag{11}$$

where Ω^h_{loc} is the domain of localized elements, **b** is the body force vector, and the surface traction **t** may be specified over some part of the boundary Γ_t^h. The weighting functions are decomposed

$$\boldsymbol{\eta}^h = \delta \mathbf{u}^h = \tilde{\boldsymbol{\eta}}^h + \hat{\boldsymbol{\eta}} \tag{12}$$

$$\begin{aligned} \nabla^{\mathrm{s}} \boldsymbol{\eta}^h = \delta \boldsymbol{\varepsilon}^h &= \nabla^{\mathrm{s}} \tilde{\boldsymbol{\eta}}^h + \nabla^{\mathrm{s}} \hat{\boldsymbol{\eta}} \\ &= \nabla^{\mathrm{s}} \tilde{\boldsymbol{\eta}}^h + \hat{\boldsymbol{\gamma}} \end{aligned} \tag{13}$$

where $\tilde{\boldsymbol{\eta}}^h$ is the conforming part of the virtual displacement, and has the same shape functions as the conforming displacements, i.e. the standard finite element shape functions. The enhanced part of the virtual displacement, $\hat{\boldsymbol{\eta}}$, has a slightly different form from the enhanced displacement to ensure compatibility, as discussed below. To ensure stability, it is necessary for these spaces to have a null intersection [54]. Since the enhancement, as discussed below, has a delta distribution, this requirement is satisfied trivially.

The first of these equations is the standard balance of linear momentum for the quasi-static, small strain kinematics. The second equation arises from the strong discontinuity and the choice of shape functions, and allows us to determine the tractions on the discontinuity surface.

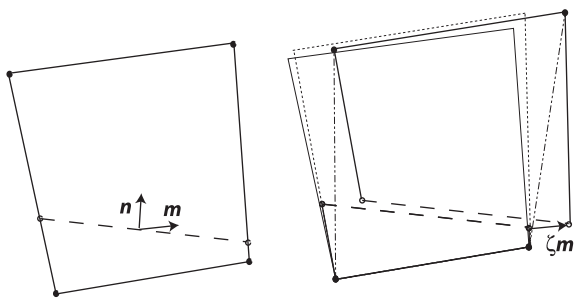

Figure 1. (a) Quadrilateral element showing potential slip surface and (b) localized element with undeformed shape (fine lines), total deformed shape (bold lines), regular deformation (dotted lines), and conforming deformation (dash-dotted lines).

DOI: 10.1002/nme

3.1. The stress on the band

Since the slip direction is prescribed and the amount of the slip is considered spatially constant across the element, there is a single extra degree of freedom, the slip, in each element. The slip rate is a function of the stress along the slip surface and the constitutive traction–displacement relationship along the surface. These constitutive models are discussed in later sections. It is Equation (11), the second equation of the Galerkin form, that allows us to determine the stress on the band. In particular, we are interested the average stress along the slip surface, which we denote $\boldsymbol{\sigma}^{\text{band}}$.

We choose as our shape function for the enhancement on an element e

$$\hat{\boldsymbol{\gamma}}_e^h = \left(\delta_S - \frac{l_S^e}{a^e}\right)(\boldsymbol{\beta}^e \otimes \mathbf{n})^{\text{s}} \tag{14}$$

where l_S^e is the length of the shear band in the element, a^e is the element area, $\boldsymbol{\beta}^e \in R^{n_{\text{sd}}}$ is the vector of weights. This function is chosen in part because it passes the patch test for piecewise constant stress fields, i.e.

$$\int_{\Omega_{\text{loc}}^h} \hat{\boldsymbol{\gamma}}\, \mathrm{d}\Omega = \mathbf{0} \tag{15}$$

Substituting (14) into (11), we obtain

$$\int_{\Omega_e} \boldsymbol{\sigma} : \left(\delta_S - \frac{l_S^e}{a^e}\right)(\boldsymbol{\beta}^e \otimes \mathbf{n})^{\text{s}}\, \mathrm{d}\Omega = \boldsymbol{\beta}^e \cdot \left(\int_S \boldsymbol{\sigma} \cdot \mathbf{n}\, \mathrm{d}S - \frac{l_S^e}{a^e}\int_{\Omega_e} \boldsymbol{\sigma} \cdot \mathbf{n}\, \mathrm{d}\Omega\right) = 0 \tag{16}$$

This implies

$$\frac{1}{a^e}\int_{\Omega_e} \boldsymbol{\sigma} \cdot \mathbf{n}\, \mathrm{d}\Omega = \frac{1}{l_S^e}\int_S \boldsymbol{\sigma} \cdot \mathbf{n}\, \mathrm{d}S = \boldsymbol{\sigma}^{\text{band}} \cdot \mathbf{n} \tag{17}$$

Hence the tractions on the band can be found by averaging those components of the stress over the element. This approximation arises from our choice of shape functions. As a mesh is refined and the element stresses approach a constant value, this approximation approaches the exact value of the stress on the element. For constant stress elements, the finite element stress is exactly recovered.

The above formulation is the small strain version of the formulation in [22]. As noted in that paper, the length of the band is never actually needed in the implementation. It is worth noting that this formulation differs slightly from [6, 36], in which

$$\hat{\boldsymbol{\gamma}}_e^h = \beta^e \left(\delta_S - \frac{l_S^e}{a^e}\right)\frac{\partial \Phi}{\partial \boldsymbol{\sigma}} \tag{18}$$

where Φ is the yield function on the surface. This formulation is also adequate, but only ensures that the stress component in the direction of $\partial\Phi/\partial\boldsymbol{\sigma}$ is equal to the average value over the element. The vector-based formulation is slightly more general, allowing for future implementation of more complex models that may have both open and sliding degrees of freedom. The numerical implementation, however, is the same for both cases.

DOI: 10.1002/nme

4. SURFACE CONSTITUTIVE MODEL

4.1. Modelling of slip weakening

Upon localization, the nature of the material changes. Instead of bulk plasticity, the inelastic slip occurs on a surface, while typically the bulk material unloads elastically. The yield condition should change to capture the weakening and the restriction of plasticity to the band. A typical model for the constitutive behaviour on the slip surface is a cohesive-frictional, or Mohr-Coulomb, form. That is, for sliding on the surface

$$\tau = c - \mu\sigma \tag{19}$$

where $\tau = \mathbf{l} \cdot \boldsymbol{\sigma} \cdot \mathbf{n}$ is the shear stress, $\mathbf{l}$ the direction of the shear traction, c the cohesion, μ the coefficient of friction, and $\sigma = \mathbf{n} \cdot \boldsymbol{\sigma} \cdot \mathbf{n}$ the normal stress on the surface. In the language of the mathematical theory of plasticity, this can be rewritten in terms of yield function

$$\Phi = \tau + \mu\sigma - c \tag{20}$$

where $\Phi<0$ implies no slip on the surface, $\Phi = 0$ is required for plastic slip, and $\Phi>0$ is inadmissible.

The coefficient of friction may vary over the course of sliding by the friction law discussed in Section 4.2 or by some other formulation. Experimental evidence and intuition both suggest that the cohesion along the surfaces rapidly degrades to zero over a short sliding distance. Exactly over what distance it degrades varies for different materials, but for quasi-brittle geomaterials this is typically on the order of 0.5 mm [55, 56].

Experiments show a shear stress drop that is approximately linear over that characteristic sliding distance, although there is some oscillation as a coherent macrocrack forms around and through the grains of the structure. A model has been developed to capture this stress drop, and is presented in [56]. Two versions of the law are presented in that paper. The first version replicates this linear drop, but requires the knowledge of $\partial\tau/\partial\sigma$ in the body as a function of the boundary conditions. For a finite element problem, this value is unknown, so a simplified version of the law is developed. The yield function on the surface takes the form

$$\Phi = \begin{cases} \tau + \mu\sigma\zeta/\zeta^{+} - \tau_0(1 - \zeta/\zeta^{+}) & \text{if } 0 \leqslant \zeta \leqslant \zeta^{+} \\ \tau + \mu\sigma & \text{if } \zeta > \zeta^{+} \end{cases} \tag{21}$$

where ζ^{+} is the characteristic sliding distance over which the resistance becomes purely frictional, and τ_0 is the shear stress at localization. Hence, the initial shear strength at localization is degraded over time as the rock fractures, and is replaced by a purely frictional resistance. The frictional strength increases over that same distance as a coherent macrocrack forms and begins slipping. If the friction is constant, then the weakening is exactly a linear function of the slip displacement. In general, however, the friction will vary during the course of slip weakening, as either the normal stress, the coefficient friction, or both change over time. The deviation from the linear law is, in most cases, rather mild.

From the above formulas, the cohesion can written as

$$c = \left(1 - \frac{\zeta}{\zeta^{+}}\right)(\tau_0 - \mu\sigma) \tag{22}$$

DOI: 10.1002/nme

This quantity is not a 'cohesion' in the traditional sense, as it varies with changing normal stress and friction coefficient. However, it is still a useful quantity in the computational setting, and is still applied.

4.2. Friction model

The functional form of the friction model used is that introduced by Ben-Zion and Rice [57]. This is a slight modification of the model presented by Dieterich and Linker [51, 58]. This latter model is based in turn on earlier work by Ruina [50], Rice and others, and has several variations by many researchers. For purposes of this discussion, however, we start with the model as presented by Dieterich and Linker.

The model is based on experimental observations that as the slip speed along two surfaces is increased instantaneously, the coefficient of friction initially increases, but then decreases to a steady-state value less than the original. A reverse process occurs when the slip speed along the two surfaces is decreased (Figure 2). The governing equation for the friction coefficient is

$$\mu = \mu^* + A \ln(V/V^*) + B \ln(\theta/\theta^*) \tag{23}$$

where V is the slip speed, θ is a state variable, and the other parameters A, B, μ^*, V^*, and θ^* are material parameters. It is worth noting that only three of the materials are independent. In other words, two of the material parameters, typically V^* and θ^*, can be assigned arbitrarily and the others determined using these values.

The state variable θ has been linked to the changing set of frictional contacts and wear on the materials [59]. Two separate evolution equations have been proposed for θ,

$$\dot{\theta} = 1 - \frac{\theta V}{D_c} \tag{24}$$

$$\dot{\theta} = -\frac{\theta V}{D_c} \ln\left(\frac{\theta V}{D_c}\right) \tag{25}$$

The first law allows for friction hardening of the material over time and is known as the healing form of the evolution equation. There is some justification for this as random movements tend to allow contacting surfaces to settle into each other over time, and experimental evidence that

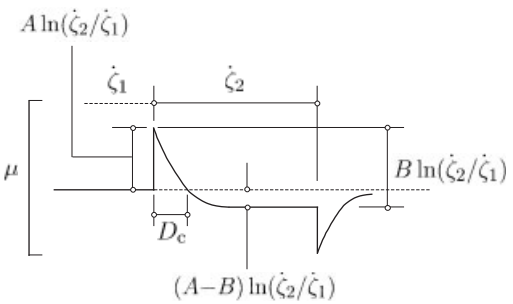

Figure 2. Coefficient of friction of the rate- and state-dependent friction model as it undergoes an instantaneous velocity increase, and then an instantaneous decrease.

DOI: 10.1002/nme

the contact area between two surfaces not in motion increases over time, even at constant normal stress [59]. Over longer time scales chemical processes may also strengthen the crack. The second equation assumes that the material does not heal in stationary contact. The material parameter D_c is referred to as the 'characteristic sliding distance.' This is the distance at which the coefficient of friction returns its former value after a velocity jump (see Figure 2). Hence, the larger the value of D_c, the more slowly the friction coefficient approaches steady state. Our implementation will focus on the healing form of the law.

For both evolution laws

$$\theta_{ss} = \frac{D_c}{V} \tag{26}$$

and hence

$$\mu_{ss}(V_2) = \mu_{ss}(V_1) + (A - B)\ln(V_2/V_1) \tag{27}$$

Since it is observed that steady-state friction decreases with increased velocity, we choose material parameters such that $A < B$.

While this model captures the varying friction coefficient under different motions well, it has the drawback that the coefficient of friction is singular at zero velocity. This difficulty can be alleviated by modifying the functional form slightly. One way to do this is to view the friction as a rate process [56, 60–62]. The details of this solution are discussed [56], but essentially one solves for the slip rate, adds in a term to account for the possibility of backward slips, and resolves for the friction coefficient. The result is

$$\mu = A \operatorname{arcsinh}\left[\frac{\dot{\zeta}}{2V^*}\exp\left(\frac{\mu^* + B\ln(\theta/\theta^*)}{A}\right)\right] \tag{28}$$

Even for mildly positive velocities, Equations (23) and (28) are nearly identical (Figure 3). The only significant difference is at zero velocity, where the coefficient of friction for the first equation

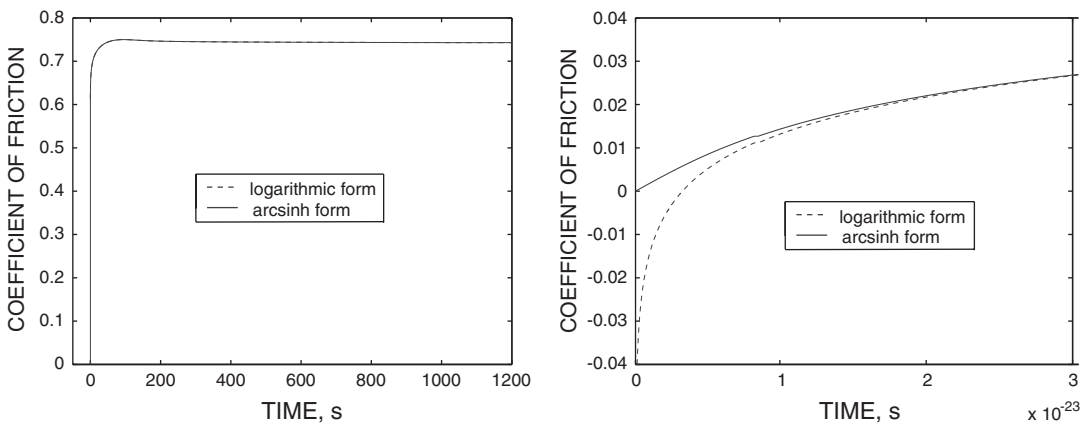

Figure 3. Comparison of friction model for typical material parameters (see Table III) for a slip rate linearly increasing from 0 at $t = 0$ s to 1 μm/s at 1000 s and then held at that speed. The models are nearly identical except for very close to the beginning (b).

DOI: 10.1002/nme

is singular while for the second equation it is zero. While even this result may seem unphysical, the slightest velocity will create a rapid movement towards a steady-state friction coefficient that is significant. In fact, the slower that velocity is, the higher the steady-state coefficient. In other words, while at zero velocity there is no resistance to movement once any motion begins, the resistance develops rapidly. Generally, then, stationary contact is replaced by almost unmeasurably slow movement.

4.3. Plastic potential

In addition to the yield function, the plastic potential must also change on localization. As shown in [33], the post-localization plastic potential, Γ, exists such that plastic strain $\boldsymbol{\varepsilon}^{\mathrm{p}}$ evolves according to

$$\dot{\boldsymbol{\varepsilon}}^{\mathrm{p}} = \lambda \frac{\partial \Gamma}{\partial \boldsymbol{\sigma}} \tag{29}$$

This is similar to bulk plasticity, but the plastic strain now takes a different form. If we assume that at post-localization all plasticity occurs on the band while the bulk material unloads elastically, then the plastic consistency parameter λ can as be written as

$$\lambda = \lambda_\delta \delta_S \tag{30}$$

Regueiro and Borja [33] show that any slip on the band is rigidly plastic. Hence, the stress rate can be written

$$\begin{aligned}
\dot{\boldsymbol{\sigma}} &= \mathbf{c}^e : (\dot{\boldsymbol{\varepsilon}} - \dot{\boldsymbol{\varepsilon}}^{\mathrm{p}}) \\
&= \mathbf{c}^e : \left[\nabla^{\mathrm{s}} \dot{\tilde{\mathbf{u}}} + (\llbracket \dot{\mathbf{u}} \rrbracket \otimes \mathbf{n})^{\mathrm{s}} \delta_S - \lambda_\delta \delta_S \frac{\partial \Gamma}{\partial \boldsymbol{\sigma}} \right] \\
&= \mathbf{c}^e : \nabla^{\mathrm{s}} \dot{\tilde{\mathbf{u}}} + \mathbf{c}^e : \left[(\llbracket \dot{\mathbf{u}} \rrbracket \otimes \mathbf{n})^{\mathrm{s}} - \lambda_\delta \frac{\partial \Gamma}{\partial \boldsymbol{\sigma}} \right] \delta_S
\end{aligned} \tag{31}$$

Since the stress rate must be bounded, this implies that

$$\begin{aligned}
\lambda_\delta \frac{\partial \Gamma}{\partial \boldsymbol{\sigma}} &= (\llbracket \dot{\mathbf{u}} \rrbracket \otimes \mathbf{n})^{\mathrm{s}} \\
&= \dot{\zeta} (\mathbf{m} \otimes \mathbf{n})^{\mathrm{s}}
\end{aligned} \tag{32}$$

If we examine this equation more closely, we see that $\dot{\zeta} \propto \lambda_\delta$, and therefore it can be used as an alternative plastic consistency parameter for the band, with $\partial \Gamma / \partial \boldsymbol{\sigma} = (\mathbf{m} \otimes \mathbf{n})^{\mathrm{s}}$. This will be convenient later, since the plastic consistency parameter now has a physical significance, and slip rate and slip distance are important parameters in many models of frictional resistance with cohesion softening. Note that this also implies

$$\dot{\boldsymbol{\sigma}} = \mathbf{c}^e : \nabla^{\mathrm{s}} \dot{\tilde{\mathbf{u}}} \tag{33}$$

In other words, the stress in the bulk material depends only on the regular part of the strain, and the slip does not affect it directly.

DOI: 10.1002/nme

5. DETERMINING THE SLIP ON THE BAND

Given the element technology discussed, and a surface constitutive model such as the one presented in Section 4, we now have the background to solve for the slip rate on the band as well as the evolution of the internal state variables. Since this solution occurs at the element level for a given global iteration, for this determination we can consider the displacements, and hence the conforming strains, as fixed. The displacements come back into play in determining the stiffness matrix for the global iteration, discussed in the next section.

Solving for the evolution of the band exactly is a difficult task. Much like bulk plasticity, the task of finding a closed-form solution is difficult if not impossible for many models. So instead we rely on numerical time integration. In this paper the approach is based on a generalized trapezoidal scheme. We will look at the numerical time integration scheme in two parts: first for a general-friction model; and second for the particular model of interest. We have found for the latter case that some simplifications can be made. In each case, we follow the spirit of the plasticity-like formulation in [33–37].

5.1. Slip on the band for a general model

Assume that at some time t_n a solution is known. We wish to solve for the condition of the band at some later time t_{n+1}. Consider a general yield condition on the band at that time

$$\Phi_{n+1} = \Phi(\zeta_{n+1}, \dot{\zeta}_{n+1}, \boldsymbol{\theta}_{n+1}, \dot{\boldsymbol{\theta}}_{n+1}) = 0 \tag{34}$$

where $(\cdot)_n$ represents the numerical solution of the variable $(\cdot)$ at time t_n, and $\boldsymbol{\theta}$ is a vector of internal state variables, each with its own well-defined evolution laws

$$\dot{\theta}^i = \dot{\Theta}^i(\zeta, \dot{\zeta}, \boldsymbol{\theta}, \dot{\boldsymbol{\theta}}) \tag{35}$$

We approach the problem using a generalized trapezoidal scheme. Given ζ_n, $\dot{\zeta}_n$, $\boldsymbol{\theta}_n$, and $\dot{\boldsymbol{\theta}}_n$, we approximate the time integration as

$$\Delta\zeta_{n+1} = \Delta t[(1 - \beta_\zeta)\dot{\zeta}_n + \beta_\zeta \dot{\zeta}_{n+1}] \tag{36}$$

$$\theta^i_{n+1} = \theta^i_n + \Delta t[(1 - \beta^i_\theta)\dot{\theta}^i_n + \beta^i_\theta \dot{\theta}^i_{n+1}] \tag{37}$$

β_ζ and β^i_θ are integration parameters, generally chosen between 0 and 1. If all these parameters are set to zero, the scheme is equivalent to explicit (forward) Euler and first-order accurate; if they are all 1 the scheme is implicit (backward) Euler and is first-order accurate; and if they are all $\frac{1}{2}$ the scheme is Crank–Nicolson and is second-order accurate. For generality, we let each variable have its own time integration parameter. This strategy may be useful, for example, if one of the variables exhibited little non-linearity and could be treated explicitly without seriously affecting the convergence of the solution. However, for second-order accuracy, β_ζ and each β^i_θ would need to be equal to $\frac{1}{2}$, and all would need to be at least $\frac{1}{2}$ to guarantee unconditional stability. It is expected that in most cases, all the time integration parameters would be set to the same value.

Whatever the values of the time integration parameters, we normally expect that ζ and $\boldsymbol{\theta}$ are easily written in terms of the other variables, and hence they can be eliminated from an iterative solution. To solve the system of equations, first we check for yielding, i.e. whether

$$\Phi(\zeta^{\text{tr}}_{n+1}, 0, \boldsymbol{\theta}^{\text{tr}}_{n+1}, \dot{\boldsymbol{\theta}}^{\text{tr}}_{n+1}) > 0 \tag{38}$$

DOI: 10.1002/nme

where $\zeta^{\mathrm{tr}}_{n+1}$ and $\boldsymbol{\theta}^{\mathrm{tr}}_{n+1}$, and $\dot{\boldsymbol{\theta}}^{\mathrm{tr}}_{n+1}$ are the values if there is no yielding at time t_{n+1}, i.e. of $\dot{\zeta}_{n+1}=0$. Clearly, $\zeta^{\mathrm{tr}}_{n+1}=\zeta_n+(1-\beta_\zeta)\dot{\zeta}_n\Delta t_{n+1}$. For a traditional plasticity-type model, where the internal state variables remain constant if there is no yielding, $\dot{\boldsymbol{\theta}}^{\mathrm{tr}}_{n+1}=0$, and $\theta^{i,\mathrm{tr}}_{n+1}=\theta^i_n+(1-\beta^i_\theta)\dot{\theta}^i_n\Delta t_{n+1}$. However, in the model discussed previously, the internal state variables do evolve even when no yielding exists.

If yielding is detected, then we must iterate to determine the final state. This can be accomplished by a standard Newton–Raphson technique. For a given set of displacements, then, we have a set of unknowns

$$\mathbf{X}_{n+1}=\begin{Bmatrix}\dot{\boldsymbol{\theta}}_{n+1}\\ \dot{\zeta}_{n+1}\end{Bmatrix} \tag{39}$$

and a corresponding number of equations

$$\mathbf{Z}=\begin{Bmatrix}\dot{\boldsymbol{\Theta}}^i(\zeta_{n+1},\dot{\zeta}_{n+1},\boldsymbol{\theta}_{n+1},\dot{\boldsymbol{\theta}}_{n+1})-\dot{\boldsymbol{\theta}}_{n+1}\\ \Phi_{n+1}\end{Bmatrix}=\mathbf{0} \tag{40}$$

with an initial guess

$$\mathbf{X}^0_{n+1}=\begin{Bmatrix}\dot{\boldsymbol{\theta}}^{\mathrm{tr}}_{n+1}\\ 0\end{Bmatrix} \tag{41}$$

We iterate by the standard formula

$$\mathbf{X}^{k+1}_{n+1}=\mathbf{X}^k_{n+1}-\left(\frac{\mathrm{D}\mathbf{Z}}{\mathrm{D}\mathbf{X}}\right)^{-1}\mathbf{Z}^k_{n+1} \tag{42}$$

until there is convergence to within some relative tolerance. The inverse here is symbolic. In the implementation a linear equation solver is used.

5.2. Slip for combined weakening and frictional model

In the case of the rate- and state-friction model of interest, we find we can use the properties of the friction model to make some simplifications, and thus reduce the computational cost of the algorithm.

The velocity on the band is unknown when checking for yielding. For zero velocity, the coefficient of friction is zero, and can go no lower (the coefficient becomes negative for negative velocities, but this is equivalent to yielding in the opposite direction). Hence, yielding occurs when

$$\Phi=(\mathbf{n}\otimes\mathbf{l})^{\mathrm{s}}:\boldsymbol{\sigma}-\tau_0\left(1-\frac{\zeta_n}{\zeta^+}\right)\geqslant 0\quad\text{if } 0\leqslant\zeta_n\leqslant\zeta^+ \tag{43}$$

For simplicity in this section, $\boldsymbol{\sigma}$ will refer to the stress on the band, $\boldsymbol{\sigma}^{\mathrm{band}}$ in previous sections. The direction of $\mathbf{l}$ is chosen such that the shear stress $(\mathbf{n}\otimes\mathbf{l})^{\mathrm{s}}$:$\boldsymbol{\sigma}$ is positive. Hence, once the residual cohesion disappears, the band yields automatically. Low shear stresses will result in far lower velocities, giving the appearance of minimal slip. It is a property of the friction model, however, that slip will occur under any condition with non-zero shear stress.

Once slip is detected, the magnitude of the slip must be determined. Since the integration over a time step is complicated, we will implement an approximate integration scheme of the generalized

DOI: 10.1002/nme

trapezoidal form. The incremental consistency condition becomes

$$\begin{aligned} 0 &= \Phi_{n+1} \\ &= [(\mathbf{n} \otimes \mathbf{l})^{\mathrm{s}} + \mu_{n+1}(\mathbf{n} \otimes \mathbf{n})] : \boldsymbol{\sigma}_{n+1} - c_{n+1} \end{aligned} \tag{44}$$

where

$$\mu_{n+1} = A \operatorname{arcsinh}\left[\frac{\dot{\zeta}_{n+1}}{2V^*} \exp\left(\frac{\mu^* + B \ln(\theta_{n+1}/\theta^*)}{A}\right)\right] \tag{45}$$

$$c_{n+1} = \begin{cases} (1 - \zeta_{n+1}/\zeta^+)(\tau_0 - \mu_{n+1}\sigma_{n+1}) & \text{if } 0 \leqslant \zeta_{n+1} \leqslant \zeta^+ \\ 0 & \text{if } \zeta_{n+1} > \zeta^+ \end{cases} \tag{46}$$

$$\boldsymbol{\sigma}_{n+1} = \boldsymbol{\sigma}_n + \mathbf{c}^e : \frac{1}{a_e} \int_{\Omega_e} [\Delta\tilde{\boldsymbol{\varepsilon}} - \Delta\zeta_{n+1}(\nabla f^h \otimes \mathbf{m})^{\mathrm{s}}] \, \mathrm{d}\Omega \tag{47}$$

After a given global iteration the displacements, and hence the conforming strains, are given. This will differ from the determination of the consistent stiffness matrix, which will be discussed later. Hence, the remaining equations become

$$\Delta\zeta_{n+1} = \Delta t[(1 - \beta_\zeta)\dot{\zeta}_n + \beta_\zeta \dot{\zeta}_{n+1}] \tag{48}$$

$$\dot{\theta}_{n+1} = 1 - \frac{\theta_{n+1}\dot{\zeta}_{n+1}}{D_{\mathrm{c}}} \tag{49}$$

$$\theta_{n+1} = \theta_n + \Delta t[(1 - \beta_\theta)\dot{\theta}_n + \beta_\theta \dot{\theta}_{n+1}] \tag{50}$$

Here again, the time integration parameters β_ζ and β_θ may be different if one wishes to treat the time evolution of the slip and internal variable in a different manner.

For this model it is not difficult to simplify the formulation and consider only a single independent variable. In this case, it is easiest to choose the slip rate $\dot{\zeta}_{n+1}$. To start, let us combine Equations (49) and (50)

$$\theta_{n+1} = \theta_n + \Delta t \left[(1 - \beta_\theta)\dot{\theta}_n + \beta_\theta \left(1 - \frac{\theta_{n+1}\dot{\zeta}_{n+1}}{D_{\mathrm{c}}}\right)\right]$$

$$\left(1 + \frac{\beta_\theta \dot{\zeta}_{n+1}\Delta t}{D_{\mathrm{c}}}\right)\theta_{n+1} = \theta_n + \Delta t[(1 - \beta_\theta)\dot{\theta}_n + \beta_\theta]$$

$$(D_{\mathrm{c}} + \beta_\theta \dot{\zeta}_{n+1}\Delta t)\theta_{n+1} = D_{\mathrm{c}}\{\theta_n + \Delta t[(1 - \beta_\theta)\dot{\theta}_n + \beta_\theta]\} \tag{51}$$

$$\theta_{n+1} = \frac{D_{\mathrm{c}}\{\theta_n + \Delta t[(1 - \beta_\theta)\dot{\theta}_n + \beta_\theta]\}}{D_{\mathrm{c}} + \beta_\theta \dot{\zeta}_{n+1}\Delta t} \tag{52}$$

The remaining variables in (44) are then functions only of $\dot{\zeta}_{n+1}$. Hence we can set up a single-variable Newton–Raphson iteration. To do this we need only derivative $\partial\Phi_{n+1}/\partial\dot{\zeta}_{n+1}$, which is given in Appendix A.

DOI: 10.1002/nme

There are two differences from the traditional implicit Euler implementation for bulk plasticity that are worth noting. First, if at time t_{n+1} there is no yielding ($\dot{\zeta}=0$), there may still be plastic slip over the step if there was yielding in the previous step and $\beta_\zeta \neq 1$. This property may be seen by examining Equation (48). For $\dot{\zeta}=0$, this becomes

$$\Delta\zeta_{n+1} = \Delta t(1-\beta_\zeta)\dot{\zeta}_n \tag{53}$$

The conforming strain increment used to check for yielding at t_{n+1} may then be different from the regular strain increment at that time.

The second note is that, since we have chosen the healing form of the evolution equations, the internal state variables evolve even over a fully elastic step. The equations for evolution for the state variable become

$$\dot{\theta}_{n+1} = 1 \tag{54}$$

$$\theta_{n+1} = \theta_n + \Delta t[(1-\beta_\theta)\dot{\theta}_n + \beta_\theta] \tag{55}$$

Note that the state variable evolves even if there is no yielding over several steps. This formulation could cause numerical problems were it not for the fact that the actual yield condition (43) is independent of θ. If this were not the case, one may have to verify convexity over stress space $\times$ loading space, which would likely be non-trivial.

We have now reduced the problem to a single-variable Newton–Raphson iteration. A summary of the algorithm appears in Box 1.

Box 1. Summary of incremental jump algorithm.

Step 1: Compute $\boldsymbol{\sigma}^{tr}_{n+1} = \boldsymbol{\sigma}_n + \mathbf{c}^e : \Delta\boldsymbol{\varepsilon}^{\text{conf}}$
Step 2: Check yielding: is $\boldsymbol{\sigma}^{tr} : (\mathbf{n}\otimes\mathbf{l}) > \tau_0(1-\zeta_n/\zeta^+)$?
If no, band is inactive. Set
$\boldsymbol{\sigma}_{n+1} = \boldsymbol{\sigma}^{tr}_{n+1}$,
$\dot{\zeta}_{n+1} = 0$,
$\Delta\zeta_{n+1} = \Delta t(1-\beta_\zeta)\dot{\zeta}_n$,
$\dot{\theta}_{n+1} = 1$,
$\theta_{n+1} = \theta_n + \Delta t[(1-\beta_\theta)\dot{\theta}_n + \beta_\theta]$,
and exit.
Step 3: Set $\dot{\zeta}^0_{n+1} = V^*$,
Step 4: Iterate
$\Delta\zeta^k_{n+1} = \Delta t[(1-\beta_\zeta)\dot{\zeta}_n + \beta_\zeta\dot{\zeta}^k_{n+1}]$
$\theta^k_{n+1} = D_c\{\theta_n + \Delta t[(1-\beta_\theta)\dot{\theta}_n + \beta_\theta]\}/(D_c + \beta_\theta\dot{\zeta}^k_{n+1}\Delta t)$
$\dot{\zeta}^{k+1}_{n+1} = \dot{\zeta}^k_{n+1} - \Phi(\dot{\zeta}^k_{n+1}, \Delta\zeta^k_{n+1}, \theta^k_{n+1})/[\partial\Phi(\dot{\zeta}^k_{n+1}, \Delta\zeta^k_{n+1}, \theta^k_{n+1})/\partial\dot{\zeta}]$
until $|\Phi^k_{n+1}|/|\Phi^0_{n+1}| < \text{tol}$
Step 5: Store $\dot{\zeta}_{n+1}$, $\Delta\zeta_{n+1}$, θ_{n+1} and $\dot{\theta}_{n+1} = 1 - \theta_{n+1}\dot{\zeta}_{n+1}/D_c$ exit.

DOI: 10.1002/nme

Remark
Although the friction model varies smoothly, the equations can be non-smooth at certain points, specifically at the yield check before the cohesion is completely degraded, and the transition from slip weakening to purely frictional response. Because of this character, a more sophisticated equation solver such as those described in [63, 64] and references cited therein may improve the efficiency and robustness of the algorithm. While the authors have not noticed any particular problems using a standard Newton iteration, the difficulties may become more pronounced if the formulation is extended to include opening degrees of freedom, creating a more contact-like scenario.

6. CONSISTENT STIFFNESS MATRIX

To solve the global finite element problem, we must form a stiffness matrix for this element. Since we have performed a numerical time integration scheme, this tangent stiffness should be consistent with the time stepping for quadratic convergence. This consistency is analogous to the consistent or algorithmic tangent modulus for continuum algorithms.

Similar to [37], we will see that the slip rate and internal state variables can be eliminated at the element level by modifying the element stiffness matrix. Hence the other element-level variables need not be added to the global solution routine, and the finite element program can solve for the displacements without modification.

6.1. Stiffness matrix for a general model

Following the implementation of a general-friction model in the previous section, we discuss here how to modify the stiffness matrix for the case of yielding. The governing equations are similar, but we now consider that the element nodes may also move, so we add the balance of linear momentum for the small strain quasi-static loading. The equations become:

$$\mathbf{r}^e = \int_{\Omega^e} \mathbf{B}^t : \boldsymbol{\sigma}\, \mathrm{d}\Omega - \int_{\Omega^e} \mathbf{N}^t \mathbf{b}\, \mathrm{d}\Omega - \int_{\Gamma^e} \mathbf{N}^t \mathbf{t}\, \mathrm{d}\Gamma = \mathbf{0} \tag{56}$$

$$\boldsymbol{\vartheta} = \dot{\boldsymbol{\Theta}}^i(\zeta_{n+1}, \dot{\zeta}_{n+1}, \boldsymbol{\theta}_{n+1}, \dot{\boldsymbol{\theta}}_{n+1}) - \dot{\boldsymbol{\theta}}_{n+1} = \mathbf{0} \tag{57}$$

$$\Phi_{n+1} = 0 \tag{58}$$

where $\mathbf{N}$ is the standard matrix of finite element shape functions, and we consider $\mathbf{B}$ here as the third-order strain–displacement tensor, i.e. $B_{ijk} d_k = \varepsilon_{ij}$. In the implementation, the corresponding matrix forms are used for computational efficiency.

Taking variations of these quantities, we arrive at

$$\delta\mathbf{r}^e = \mathbf{K}^e_{dd}\delta\mathbf{d}^e + \mathbf{K}^e_{d\dot{\theta}}\delta\dot{\boldsymbol{\theta}} + \mathbf{K}^e_{d\dot{\zeta}}\delta\dot{\zeta} \tag{59}$$

$$\delta\boldsymbol{\vartheta} = \mathbf{K}^e_{\dot{\theta}d}\delta\mathbf{d}^e + \mathbf{K}^e_{\dot{\theta}\dot{\theta}}\delta\dot{\boldsymbol{\theta}} + \mathbf{K}^e_{\dot{\theta}\dot{\zeta}}\delta\dot{\zeta} \tag{60}$$

$$\delta\Phi = \mathbf{K}^e_{\dot{\zeta}d}\delta\mathbf{d}^e + \mathbf{K}^e_{\dot{\zeta}\dot{\theta}}\delta\dot{\boldsymbol{\theta}} + K^e_{\dot{\zeta}\dot{\zeta}}\delta\dot{\zeta} \tag{61}$$

DOI: 10.1002/nme

The first quantity, $\mathbf{K}^e_{dd}$, is the standard element stiffness matrix. The four parts of the stiffness comprising the lower right-hand portion

$$\mathbf{K}^e_{\dot{\theta}\dot{\theta}} = \frac{\partial \dot{\vartheta}}{\partial \dot{\boldsymbol{\theta}}} \tag{62}$$

$$\mathbf{K}^e_{\dot{\theta}\dot{\zeta}} = \frac{\partial \dot{\vartheta}}{\partial \dot{\zeta}} \tag{63}$$

$$\mathbf{K}^e_{\dot{\zeta}\dot{\theta}} = \frac{\partial \dot{\Phi}}{\partial \dot{\boldsymbol{\theta}}} \tag{64}$$

$$K^e_{\dot{\zeta}\dot{\zeta}} = \frac{\partial \dot{\Phi}}{\partial \dot{\zeta}} \tag{65}$$

are the same quantities used to determine the slip on the band, and the same code can be reused. The final four quantities are

$$\mathbf{K}^e_{d\dot{\theta}} = \frac{\partial \mathbf{r}^e}{\partial \dot{\boldsymbol{\theta}}} \tag{66}$$

$$\mathbf{K}^e_{d\dot{\zeta}} = \frac{\partial \mathbf{r}^e}{\partial \dot{\zeta}} = -\int_{\Omega^e} \mathbf{B}^t : \mathbf{c}^e : (\nabla f^h_e \otimes \mathbf{m})^{\mathrm{s}} \, \mathrm{d}\Omega \beta_\zeta \Delta t \tag{67}$$

$$\mathbf{K}^e_{\dot{\theta}d} = \frac{\partial \dot{\vartheta}}{\partial \mathbf{d}^e} \tag{68}$$

$$\mathbf{K}^e_{\dot{\zeta}d} = \frac{\partial \dot{\Phi}}{\partial \dot{\zeta}} \tag{69}$$

Most of the quantities above depend on the constitutive response and cannot be specified further in this section. In some cases, we can provide more information. For example, if the state variables are only affected by the nodal displacements through the stress, then

$$\mathbf{K}^e_{\dot{\theta}d} = \frac{\partial \dot{\boldsymbol{\theta}}}{\partial \boldsymbol{\sigma}} : \frac{\partial \boldsymbol{\sigma}}{\partial \mathbf{d}^e} = \frac{1}{a^e} \int_{\Omega^e} \frac{\partial \dot{\boldsymbol{\theta}}}{\partial \boldsymbol{\sigma}} : \mathbf{c}^e : \mathbf{B}^e \, \mathrm{d}\Omega \tag{70}$$

Finally, we note that, since the state variables and the slip rate are element quantities that do not affect surrounding elements, we can statically condense the stiffness matrix, following Borja and Regueiro [37]

$$\mathbf{K}^e = \mathbf{K}^e_{dd} - [\mathbf{K}^e_{d\dot{\theta}} \;\; \mathbf{K}^e_{d\dot{\zeta}}] \begin{bmatrix} \mathbf{K}^e_{\dot{\theta}\dot{\theta}} & \mathbf{K}^e_{\dot{\theta}\dot{\zeta}} \\ \mathbf{K}^e_{\dot{\zeta}\dot{\theta}} & K^e_{\dot{\zeta}\dot{\zeta}} \end{bmatrix}^{-1} \begin{bmatrix} \mathbf{K}^e_{\dot{\theta}d} \\ \mathbf{K}^e_{\dot{\zeta}d} \end{bmatrix} \tag{71}$$

DOI: 10.1002/nme

The great advantage of this strategy is that all variables except the nodal displacements are condensed out at the element level, so the global solution algorithm can simply input the element stiffness matrix (71) with no modification.

6.2. *Stiffness matrix for combined weakening and frictional model*

Once the jump increment and internal state variable θ have been solved for a given set of displacements, the tangent stiffness matrix consistent with this algorithm falls out with relatively little modification if we follow [37]. Two conditions must be met

$$\mathbf{r}^e = \int_{\Omega^e} \mathbf{B}^t : \boldsymbol{\sigma}\, \mathrm{d}\Omega - \int_{\Omega^e} \mathbf{N}^t \mathbf{b}\, \mathrm{d}\Omega - \int_{\Gamma^e} \mathbf{N}^t \mathbf{t}\, \mathrm{d}\Gamma = 0 \tag{72}$$

$$\Phi_{n+1} = 0 \tag{73}$$

Since we now have only the variables $\mathbf{d}$ and $\dot{\zeta}$ as independent, taking a variation on these equations results in

$$\delta \mathbf{r}^e = \mathbf{K}^e_{dd} \delta \mathbf{d}^e + \mathbf{K}^e_{d\dot{\zeta}} \delta \dot{\zeta}^e \tag{74}$$

$$\delta \Phi = \mathbf{K}^e_{\dot{\zeta}d} \delta \mathbf{d}^e + \mathbf{K}^e_{\dot{\zeta}\dot{\zeta}} \delta \dot{\zeta}^e \tag{75}$$

where

$$\mathbf{K}^e_{dd} = \int_{\Omega^e} \mathbf{B}^t : \mathbf{c}^e : \mathbf{B}\, \mathrm{d}\Omega \tag{76}$$

$$\mathbf{K}^e_{d\dot{\zeta}} = -\int_{\Omega^e} \mathbf{B}^t : \mathbf{c}^e : (\nabla f^h_e \otimes \mathbf{m})^{\mathrm{s}}\, \mathrm{d}\Omega \beta_{\zeta} \Delta t \tag{77}$$

$$\mathbf{K}^e_{\dot{\zeta}d} = \frac{\partial \Phi}{\partial \mathbf{d}} \tag{78}$$

$$\mathbf{K}^e_{\dot{\zeta}\dot{\zeta}} = \frac{\partial \Phi}{\partial \dot{\zeta}} \tag{79}$$

The last quantity we already have. The third quantity is

$$\frac{\partial \Phi}{\partial \mathbf{d}} = \frac{1}{a^e} \int_{\Omega^e} \frac{\partial \Phi}{\partial \boldsymbol{\sigma}} : \mathbf{c}^e : \mathbf{B}\, \mathrm{d}\Omega \tag{80}$$

$$= \begin{cases} (a^e)^{-1} \displaystyle\int_{\Omega^e} \left[(\mathbf{n} \otimes \mathbf{l})^{\mathrm{s}} + \frac{\zeta}{\zeta^+} \mu (\mathbf{n} \otimes \mathbf{n}) \right] : \mathbf{c}^e : \mathbf{B}\, \mathrm{d}\Omega & \text{if } \zeta \leqslant \zeta^+ \\ (a^e)^{-1} \displaystyle\int_{\Omega^e} [(\mathbf{n} \otimes \mathbf{l})^{\mathrm{s}} + \mu (\mathbf{n} \otimes \mathbf{n})] : \mathbf{c}^e : \mathbf{B}\, \mathrm{d}\Omega & \text{if } \zeta > \zeta^+ \end{cases} \tag{81}$$

DOI: 10.1002/nme

where the subscripts $n+1$ have been omitted for convenience. As before, the slip rate can be statically condensed out, and the resulting element stiffness matrix is

$$\mathbf{K}^e = \mathbf{K}^e_{dd} - \mathbf{K}^e_{d\dot{\zeta}} K^{e\,-1}_{\dot{\zeta}\dot{\zeta}} \mathbf{K}^e_{\dot{\zeta}d} \tag{82}$$

7. BAND TRACKING ALGORITHM

The band tracking strategy employed is of the type that Oliver and coworkers have termed a local strategy. This method is in contrast to a global strategy described in [30, 31] or level set methods employed in [44]. The idea is to track the band as it propagates from element to element, explicitly keeping track of the co-ordinates where the band intersects an element edge.

Prior to the onset of localization, the bifurcation condition is checked at the end of each time step. Once localization is detected in at least one element, the band tracking begins. First, a root element must be determined. Usually, we specify the element that has the least value of $\det \mathbf{Q}$ as the first root element. However, for special cases such as homogeneous deformation, we choose a root element or elements. For homogeneous deformation, all the elements bifurcate at the same time. In reality though, some perturbation will trigger earlier localization in some location or locations, which for the sake of those problems we choose.

Once a root element is detected, that element is traced through the centroid using the critical normal, and the endpoints of the band are calculated and recorded. To determine the points of intersection, we note that the edges intersected by the discontinuity are those with an active node at one end and an inactive node at the other. Since the active nodes are already needed to determine the function f^h, it is computationally trivial to loop over the edges to find the edges of intersection. Assuming the element edges are straight, the intersection point $\mathbf{x}$ can be determined from the system of equations

$$\mathbf{x} = \mathbf{x}^e_{\mathrm{s}} + \alpha \mathbf{l} \tag{83}$$

$$\mathbf{x} = \beta(\mathbf{x}^e_a - \mathbf{x}^e_b) \tag{84}$$

where $\mathbf{x}^e_a$ and $\mathbf{x}^e_b$ are the co-ordinates end nodes of that edge, $\mathbf{x}^e_{\mathrm{s}}$ are the co-ordinates of a point on discontinuity surface, and α and β are initially undetermined scalars. the vector $\mathbf{x}^e_{\mathrm{s}}$ is taken to be the centroid of the element for a root element, otherwise it is the point of intersection of the edge and failure surface from the adjacent element. By substituting the value of $\mathbf{x}$ from (84) into (83), and then solving that system of two equations for α, we get

$$\alpha = \frac{\|(\mathbf{x}^e_a - \mathbf{x}^e_b) \times (\mathbf{x}^e_{\mathrm{s}} - \mathbf{x}^e_a)\|}{\|\mathbf{l} \times (\mathbf{x}^e_a - \mathbf{x}^e_b)\|} \tag{85}$$

Once α is determined, we can use Equation (83) to solve for the point of intersection.

The next elements we check are those that are adjacent to the root element at the end of the band. If these elements have localized, we want to ensure that the band is continuous across element boundaries. To find these elements, we construct an element neighbours (EN) array from the standard internal entry number (IEN), or element nodes array [65]. This array is constructed such that $\mathrm{EN}(i, j)$ is the number of the element adjacent to element i at local face j. If there is no neighbour there, i.e. that face is at the boundary of the body, then -1 is returned.

We use active and passive nodes of the element to locate the local edge that contains the band. Looping over the edges of an element i, if we find an edge j between an active and a passive

DOI: 10.1002/nme

node, then we check that

(1) the EN array does not return -1;
(2) the element number is not already in the edge-of-band-elements array, and
(3) the element is not already traced.

If all these criteria are satisfied, we add the element number EN(i, j) to a variable length edge-of-band-elements array along with the co-ordinates of the end of the band.

We then go to the first element in the edge-of-band-elements array and check for localization. If localization is detected we trace that element, find the new neighbour, and add it to the end of the array. We then proceed to the next element, and so forth until we reach the end of the array, which may be growing throughout the tracking process.

If we are fairly certain that one band will form, we can stop there, and at subsequent time steps only check the elements in the edge-of-band-elements array. If we allow for the possibility of multiple bands, however, we now check the remaining elements for localization. If other elements have been localized, we determine a new root element, and propagate a new band in the same way. We can use a single edge-of-band-elements array for this process.

At subsequent time steps, it is important to check for elements in the edge-of-band-elements array before proceeding to check for new root elements. This ensures that newly localized elements are added to existing bands. The algorithm is summarized in Box 2.

Box 2. Summary of band tracking algorithm, performed at the end of each time step.

Step 1: If localization has not begun, check for localization, of all elements. If localization is detected, choose element with the least value of det $\mathbf{Q}$, and perform *localize* subroutine. If not, exit.

Step 2: Move to first element of edge-of-band-elements array. If the array is empty, exit. Otherwise, go to step 3.

Step 3: Check for localization of element in array. If localization detected, perform *localize* subroutine and delete from array.

Step 4: Move to next element in array. If at the end, exit. Otherwise, go to step 3.

Step 5: If allowing for multiple bands: check for remaining, untraced elements that may have localized. If localization is detected, choose element with least value of det $\mathbf{Q}$, and perform *localize* subroutine and go to step 3. If not, exit.

localize subroutine
Step 1: Trace element according to normal and co-ordinate (either from information in edge-of-band-elements array or centroid)

Step 2: Go to first element edge.

Step 3: If current edge has one active and one inactive end node *and* neighbour element exists *and* that element has not yet been traced *and* that element is not already in the edge-of-band elements array, determine co-ordinates of intersection of band and element edge, and add to edge-of-band-elements array.

Step 4: If all edges have been check or both ends of band have been found, exit. Otherwise, go to step 3.

DOI: 10.1002/nme

8. NUMERICAL EXAMPLES

8.1. Sliding of a pre-fractured block

The first example consists of a 1-meter × 1-meter block, discretized into nine elements, and with a strong discontinuity inserted horizontally through the centre. The exaggerated conforming deformations are shown in Figure 4. The mesh was then refined to 81 elements. As the sample is pre-fractured, the initial shear stress is zero. The ability to pre-fracture a sample was added to the code to test the convergence of the friction algorithm and to verify the properties of the friction model.

The material properties are listed in Table I. These properties are taken to simulate a granite, with most of the frictional properties taken from [51], except for μ^* and the elastic properties, which are taken from typical values for granite.

As Figure 5 shows, the finite element model captures the variation in the coefficient of friction exhibited by the friction model. As motion starts, the friction coefficient rapidly rises and dips to steady state. We might expect a faster rise in the friction coefficient, but there is comparitively

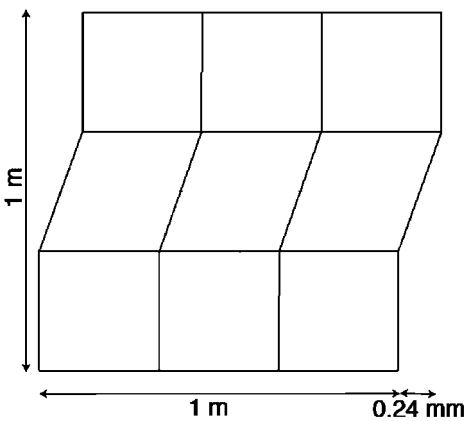

Figure 4. Deformed shape for example 1 showing conforming displacements, multiplied 100 times. The failure surface passes horizontally through the centre of the three centre elements. Since the global finite element needs no information about the band, the postprocessor uses standard nodal interpolations.

Table I. Material properties for granite direct shear test.

Parameter	Symbol	Value
Young's modulus	E	5500 MPa
The Poisson ratio	v	0.25
Reference friction coefficient	μ^*	0.72
Velocity variation coefficient	A	0.0012
State variable variation coefficient	B	0.00135
Velocity normalizing constant	V^*	1.0 μm/s
State variable normalizing constant	θ^*	2.25
Characteristic sliding distance	D_c	μm

DOI: 10.1002/nme

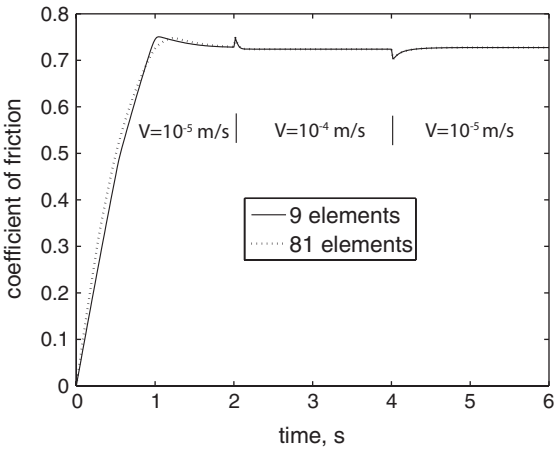

Figure 5. Coefficient of friction as a function of time under the prescribed displacements for direct shear example.

Table II. Error as a function of the number of time steps at 4.2 s.

Number of time steps	Explicit Euler	Crank–Nicolson	Implicit Euler
30	*	*	3.0431E−0
300	*	1.1540E−03	6.6593E−04
3000	7.8128E − 05	1.1749E−06	7.1984E−05

Note: Error calculated using an 'exact' solution of 30 000 time steps with the Crank–Nicolson scheme. Entries with a * did not converge.

little shear stress to drive this rise initially. As the slip speed is increased, the characteristic spike and drop to a lower steady-state value are seen. Similarly, when the velocity is dropped again, the coefficient of friction dips and then rises to a new, higher value. The elastic parameters are quite stiff compared to the frictional parameters, and hence the elasticity plays little role in the material behaviour after the initial rise. The refinement shows results that are quite comparable to the initial run. The response is initially slightly stiffer, but shows less of a peak in the initial rise. Once the friction reaches steady state for the first time, the solutions are nearly identical.

Table II shows the convergence rate for the various methods, using the coefficient of friction as the parameter of interest. We use a time of 4.2 s, when the friction coefficient is still changing, as our gauge. At the end of the run, the solution is too close to steady state and the convergence rates tend to look better than the methods would predict. Explicit Euler, Crank–Nicolson, and Implicit Euler runs were each made with time steps of 0.2, 0.02, and 0.002 s. The 'exact' solution was then obtained by running a Crank–Nicolson simulation with a time step of 0.0002 s.

Not surprisingly, the explicit simulation diverged for large time steps. Only the last run converged, leaving no comparisons to check the convergence rate. However, the error is of the same order as the implicit Euler run for that time step, which suggests that the method is behaving as expected. Implicit Euler shows the expected first-order convergence, while the Crank–Nicolson scheme shows convergence slightly faster than second-order rate would predict. The Crank–Nicolson simulation

DOI: 10.1002/nme

with a time step of 0.2 s failed to converge in a Newton iteration, which is not related to the stability of the problem. This problem could have been solved by step cutting, but this process would affect the error.

8.2. Plane strain compression of a laboratory sample

The second example is a plane strain compression simulation of San Marcos gabbro. This test is meant to recreate a two-dimensional version of the triaxial test G3 described in Wong [66] in the slip weakening stage. The simulation was initially reported in [56]. The material parameters are shown in Table III. The elastic parameters are taken from typical values for gabbro. The plasticity model is a Drucker–Prager model with linear hardening (here, softening). The parameters are set to reproduce, to the best of the information given, the forces measured in the experiment. The reference friction coefficient μ^* is taken to satisfy the recorded strength and failure geometry from the experiments. The remaining friction parameters are from a granite sample discussed in [51]. A confining pressure of 250 MPa is applied to the sides, and then the sample is compressed vertically.

The results are shown in Figures 6 and 7. The specimen at first behaves elastically, then plastically until bifurcation is detected. Since the deformation is homogeneous, a seed element is chosen in the middle and a single band propagates from that element. For these material properties, the failure surface forms at 60° from the horizontal, but could form in either direction. The choice of band direction is made by an algorithm as described in [34], but in this case both choices are equally likely. In a physical specimen the direction of propagation would be chosen by flaws or slight variations in the material properties. Since we do not have information at that level for our simulation and the direction is not important for our study, we let the algorithm choose the normal based on machine roundoff error.

Once the surfaces are inserted, the sample unloads under slip weakening. The experimental information concludes noting only a final friction coefficient. However, to demonstrate the properties of the friction model at post-weakening, we add a velocity jump to the simulation. Initially, the vertical compression rate is 0.866 μm/s, which at steady-state slipping would give a slip velocity of 1 μm/s on the band. However, some unstable slip occurs at first that otherwise would not be

Table III. Material properties for plane strain compression of San Marcos gabbro.

Parameter	Symbol	Value
Young's modulus	E	5500 MPa
The Poisson ratio	ν	0.25
Cohesive strength parameter	α	8.034 MPa
Friction parameter	β	0.633
Dilation parameter	b	0.633
Hardening modulus	H	−10 MPa
Reference friction	μ^*	0.72
Velocity variation coefficient	A	0.0012
State variable variation coefficient	B	0.00135
Velocity normalizing constant	V^*	1.0 μm/s
State variable normalizing constant	θ^*	2.25
Characteristic sliding distance	D_c	μm/s

DOI: 10.1002/nme

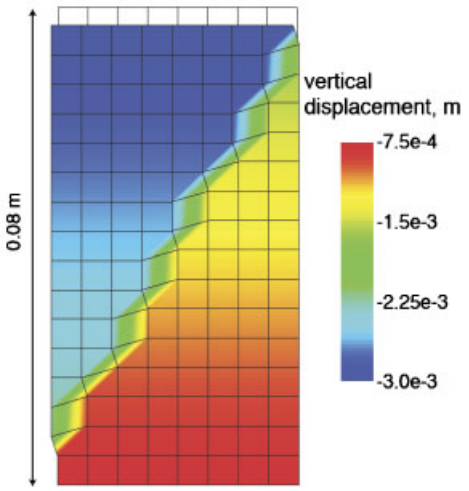

Figure 6. Deformed shape at the end of simulation for plane strain compression example. Black outline in background shows initial configuration.

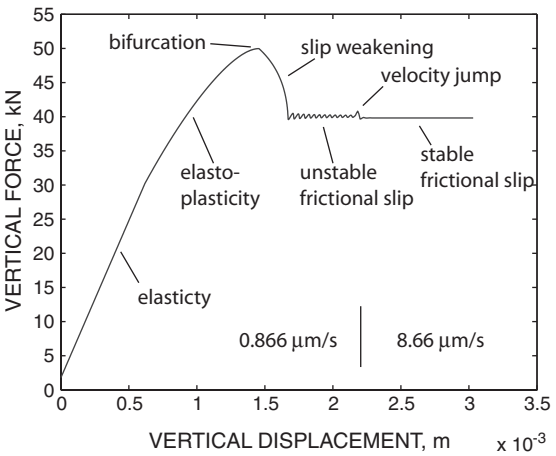

Figure 7. Force–displacement curve for plane strain compression showing behaviour in different stages of deformation.

predicted by rigid block models. This slip is a function of the stiffness of the sample and the friction parameters, and is analogous to the spring-slider examples discussed in [50]. A velocity step is added at 2 mm total vertical displacement, resulting in the jump and subsequent dip of the friction coefficient. At the higher speed that is 10 times the initial rate, slip rapidly becomes stable, again as predicted by the model.

This problem was run with 1, 15, and 128 elements. Since the problem is homogeneous, it is not surprising that the solutions are nearly identical. The relative error in the vertical force

DOI: 10.1002/nme

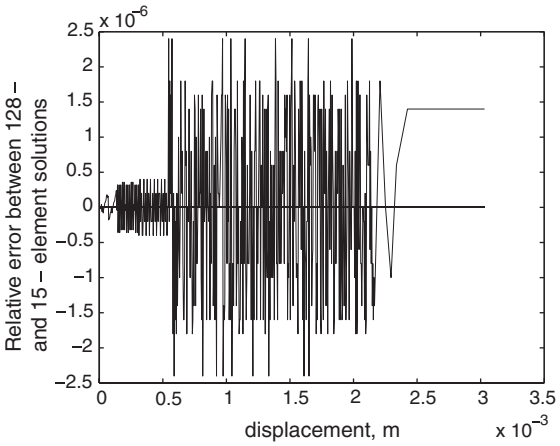

Figure 8. Relative error in force between 15- and 128-element solution as a function of time. The error is a result of the tolerance in the iterations, and the solution of the global equations. The error in the plastic and localized phases is comparable.

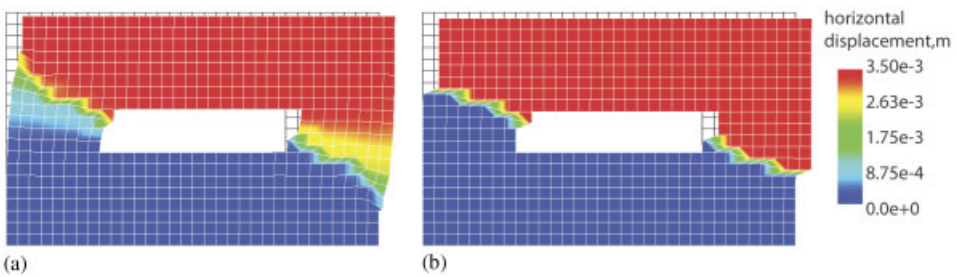

Figure 9. Deformed shape of the shear example with a hole, 576-element case. (a) when the band is allowed to propagate in the critical direction, locking effects lead to additional bulk plasticity and new bands. Note the increased bulk dilation over (b) where the sample unloads elastically after the straight band propagates. Undeformed shape shown in background in black outline.

between the 15- and 128-element solutions is shown in Figure 8. The error in the localized phase is similar to that in the plastic phase. This error is due to the convergence tolerance in the local and element-level solutions, and the solution of the global system of equations.

8.3. Shearing of sample with a hole

As we move to more complex problems, some interesting issues arise. We start by simulating the shearing of an 80- $\times$ 100-cm block with a hole in it as shown in Figure 9 to test the tracking of multiple bands. In this case the friction coefficient is constant, and material properties are listed in Table IV.

The initial results show that the band propagates through the sample and initially there is significant softening (see Figure 10), but this is followed by hardening. This hardening is due to

DOI: 10.1002/nme

Table IV. Material properties for shear example with hole.

Parameter	Symbol	Value
Young's modulus	E	9000 MPa
The Poisson ratio	ν	0.15
Cohesive strength parameter	α	8.034 MPa
Friction parameter	β	0.633
Dilation parameter	b	0.3165
Hardening modulus	H	0 MPa
Friction coefficient	μ	0.6

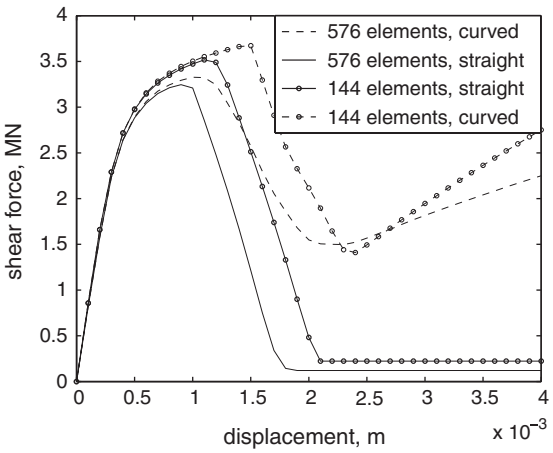

Figure 10. Force–displacement curve for shearing of example with hole in it. If the band is forced to propagate in a straight line, the resistance drops to a purely frictional response. If the band is allowed to propagate in the critical direction, it initially softens, but locking effects due to the changing direction eventually create hardening.

a locking effect as surfaces in adjacent elements attempt to slip in different directions. To some extent, this reflects a physical process in that changing directions on surfaces do create an increased resistance to slip. Elements with opening and perhaps rotational degrees of freedom to the surface, such as [30, 48], could change the kinematics of slip, allowing for local areas of opening. For comparison, we also rerun the problem but force the band to propagate in a straight line. In this case the sample softens to a purely frictional response, and little bulk plasticity is seen in the rest of the sample. The original simulation shows significant bulk plasticity, including dilation, and even creates newly localized bands (these new bands do not slip very much and hence are not visible in the deformed shape).

The problem is run with 144 and 576 elements. The response is slightly softer for the 576-element case, but similar. The refined mesh naturally detects plasticity and localization earlier, as there are more points to sample. In the straight band case, the initial angle of the band is slightly more vertical, resulting in a lower frictional response. In the curved band case, the refinement shows slightly less softening before the stress locking occurs, but the residual slope is lower.

DOI: 10.1002/nme

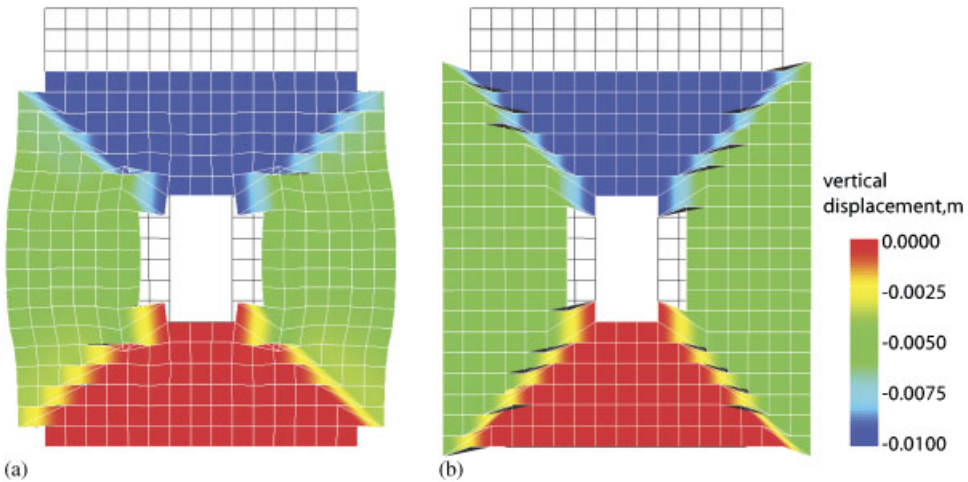

Figure 11. Deformed shape for compression of sample with hole in it, 336-element case. (a) Bulk plasticity increases after the curving band locks up, while (b) the straight band allows for elastic unloading of the bulk sample. Undeformed shape shown in background in black outline.

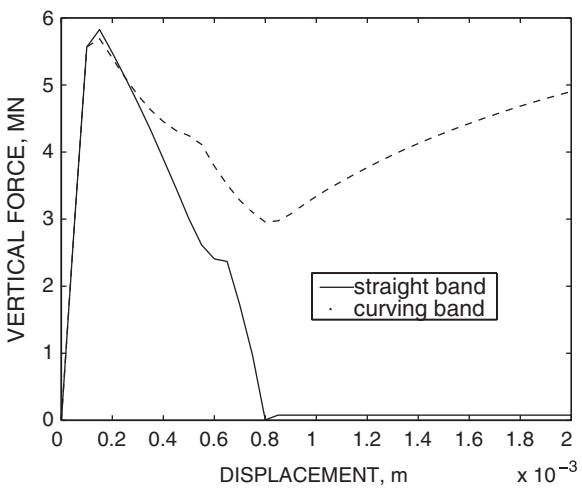

Figure 12. Force–displacement curve for compression of example with hole in it, 336-element case. If the band is forced to propagate in a straight line, the resistance drops to a purely frictional response. If the band is allowed to propagate in the critical direction, it initially softens, but locking effects due to the changing direction eventually create hardening.

8.4. Compression of sample with a hole

We also run a compression test of a 50- × 70-cm sample with a hole in it as shown in Figure 11. The frictional variation is the same as the San Marcos gabbro sample. When compressed, bands propagate from the interior corners of the sample. Similar to the shear example, if the band

DOI: 10.1002/nme

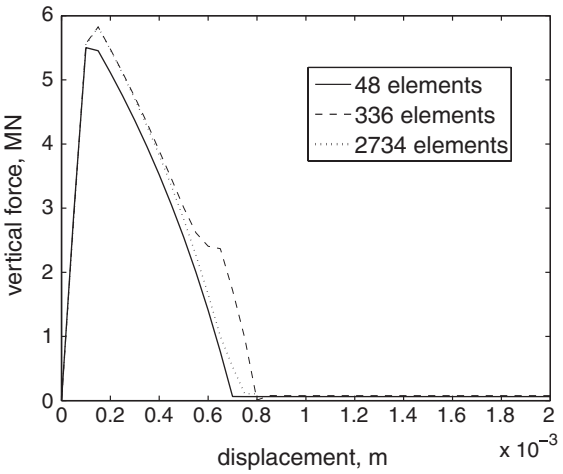

Figure 13. Results of mesh refinement for compression example with a hole in it for straight band. The results appear to converge. The only significant difference between the 336- and 2734-element solutions is one point in the 336-element solution where the band stops propagating momentarily.

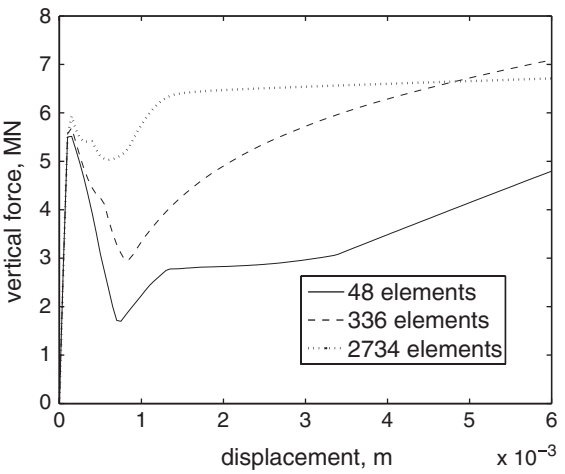

Figure 14. Results of mesh refinement for compression example with a hole in it for curving band. As the mesh is refined, locking occurs earlier, but the residual slope of the force–displacement curve decreases.

is allowed to change direction in different elements, there is a locking effect after some initial softening. The locking results again in significant bulk deformation and plasticity later on in the deformation process. Again, if the bands are forced to propagate in a straight line, the sample unloads elastically after bifurcation. A comparison of the force–displacement responses is shown in Figure 12.

DOI: 10.1002/nme

Mesh refinements show similar responses. The problem was run with 48-, 336-, and 2734-element meshes. For the straight band case (Figure 13) the only significant difference between the 336- and 2734-element meshes is that band seems to stop propagating for a couple steps in the 336-element case. This behaviour disappears upon refinement. In the curved band case (Figure 14) locking shows up sooner, as may be expected when the elements are smaller, but the residual slope of the force–displacement curve is less.

9. CONCLUSIONS

In this paper we have presented a novel algorithm for implementing a general traction–displacement model into an enhanced strain element. The specific model considered combines slip weakening during nucleation of a strong discontinuity and frictional response appropriate for geomaterials and other materials exhibiting velocity- and state-dependent coefficient of friction. The constitutive model chosen in this paper to represent a variable coefficient of friction applies to slow slip velocities and laboratory-derived state and friction laws, where variations in the coefficient of friction are generally small. However, for large slips and slip rates, a much lower coefficient of friction may be activated by additional weakening mechanisms such as flash heating [62, 67]. The framework presented in this paper is a first step towards implementing such friction models, including those encountered in earthquake fault modelling. Work in this area is in progress.

Numerical examples demonstrate that the formulation converges at the rate mathematical analysis predicts. They also demonstrate some of the advantages of implementing this element into a continuum framework such as the finite element method. Such a formulation can predict the direction and timing of crack propagation through a body as the forces redistribute. It also endows the body with a finite stiffness, which is critical for determining whether the slip along the surface is stable or unstable. A rigid approximation of the bulk material would be unable to predict these conditions.

Finally, a locking effect occurs when bands change direction as they propagate. While some of this may be physical, additional enhancements may be needed to overcome the additional resistance that the formulation artificially generates, such as that arising from an opening crack mode.

APPENDIX A: DERIVATIVE OF THE YIELD FUNCTION

For completeness, we include the derivative of the time-discretized post-localization yield function (44) with respect to the slip rate:

$$\frac{\partial \Phi_{n+1}}{\partial \dot{\zeta}_{n+1}} = [(\mathbf{n}\otimes\mathbf{l})^{\mathrm{s}} + \mu_{n+1}(\mathbf{n}\otimes\mathbf{n})] : \frac{\partial \boldsymbol{\sigma}_{n+1}}{\partial \dot{\zeta}_{n+1}} + \frac{\partial \mu_{n+1}}{\partial \dot{\zeta}_{n+1}}(\mathbf{n}\otimes\mathbf{n}) : \boldsymbol{\sigma}_{n+1} - \frac{\partial c_{n+1}}{\partial \dot{\zeta}_{n+1}} \tag{A1}$$

where

$$\frac{\partial c_{n+1}}{\partial \dot{\zeta}_{n+1}} = \begin{cases} -x - y & \text{if } 0 \leqslant \zeta_{n+1} \leqslant \zeta^{+} \\ 0 & \text{if } \zeta_{n+1} > \zeta^{+} \end{cases} \tag{A2}$$

DOI: 10.1002/nme

and

$$x = \left(1 - \frac{\zeta_{n+1}}{\zeta^+}\right)\left(\sigma_{n+1}\frac{\partial \mu_{n+1}}{\partial \dot{\zeta}_{n+1}} + \mu_{n+1}\frac{\partial \sigma_{n+1}}{\partial \dot{\zeta}_{n+1}}\right) \tag{A3}$$

$$y = \frac{(\partial \zeta_{n+1}/\partial \dot{\zeta}_{n+1})}{\zeta^+}(\tau_0 - \mu\sigma_{n+1}) \tag{A4}$$

$$\frac{\partial \Delta\zeta_{n+1}}{\partial \dot{\zeta}_{n+1}} = \beta_\zeta \Delta t \tag{A5}$$

$$\frac{\partial \boldsymbol{\sigma}_{n+1}}{\partial \dot{\zeta}_{n+1}} = -\mathbf{c}^e : (\nabla f^h \otimes \mathbf{m})\frac{\partial \Delta\zeta_{n+1}}{\partial \dot{\zeta}_{n+1}} \tag{A6}$$

If we define

$$\alpha = \frac{1}{2V^*}\exp\left(\frac{\mu^* + B\ln(\theta_{n+1}/\theta^*)}{A}\right) \tag{A7}$$

then

$$\begin{aligned}\frac{\partial \mu_{n+1}}{\partial \dot{\zeta}_{n+1}} &= \frac{A}{\sqrt{1 + (\dot{\zeta}_{n+1}\alpha)^2}} * \left(\alpha + \dot{\zeta}_{n+1}\alpha\frac{B}{A\theta}\frac{\partial \theta_{n+1}}{\partial \dot{\zeta}_{n+1}}\right) \\ &= \frac{A\alpha}{\sqrt{1 + (\dot{\zeta}_{n+1}\alpha)^2}} * \left(1 + \frac{\dot{\zeta}_{n+1}B}{A\theta_{n+1}}\frac{\partial \theta_{n+1}}{\partial \dot{\zeta}_{n+1}}\right)\end{aligned} \tag{A8}$$

$$\frac{\partial \theta_{n+1}}{\partial \dot{\zeta}_{n+1}} = -\frac{\beta_\theta \Delta t\, D_c\{\theta_n + \Delta t[(1-\beta_\theta)\dot{\theta}_n + \beta_\theta]\}}{(D_c + \beta_\theta \dot{\zeta}_{n+1}\Delta t)^2} \tag{A9}$$

ACKNOWLEDGEMENTS

The authors would like to thank Patrick Klein for his generous assistance in helping with code issues. We also would like to thank Professors D.D. Pollard and J.R. Rice for discussions on fundamental behaviour of geomaterials, and for providing several relevant references. The first and second authors acknowledge the support of the U.S. National Science Foundation, Grant No. CMG-0417521 (Collaborations in Mathematical Geosciences).

The first author would like to acknowledge the Sandia National Laboratories LDRD program, Sandia's Engineering Summer Sciences Internship Program, and the Swanson Foundation Achievement Rewards for College Scientists Stanford Graduate Fellowship.

The second author acknowledges the support of the U.S. Department of Energy Grant No. DE-FG02-03ER15454.

The third author also would like to acknowledge the Sandia National Laboratories LDRD program.

DOI: 10.1002/nme

REFERENCES

1. Rudnicki JW, Rice JR. Conditions for the localization of deformation in pressure-sensitive dilatant materials. *Journal of the Mechanics and Physics of Solids* 1975; **23**(6):371–394.
2. Borja RI. Conditions for instabilities in collapsible solids including volume implosion and compaction banding. *Acta Geotechnica* 2006; **1**(2):107–122.
3. Wriggers P. *Computational Contact Mechanics*. Wiley: Chichester, 2002.
4. Laurson TA. *Computational Contact and Impact Mechanics*. Springer: Berlin, New York, Heidelberg, 2002.
5. Klein PA, Foulk JW, Chen EP, Wimmer SA, Gao HJ. Physics-based modelling of brittle fracture: cohesive formulations and the application of meshfree methods. *Theoretical and Applied Fracture Mechanics* 2001; **37**(1/3):99–166.
6. Regueiro RA, Fossum AF, Jensen RP, Foster CD, Manzari MT, Borja RI. *Computational Modelling of Fracture and Fragmentation in Geomaterials*. SAND2005-5940, Sandia National Laboratories, 2005.
7. Needleman A. Material rate dependence and mesh sensitivity in localization problems. *Computer Methods in Applied Mechanics and Engineering* 1988; **67**:69–85.
8. Abed FH, Voyiadjis GZ. Plastic deformation modelling of AL-6XN stainless steel at low and high strain rates and temperatures using a combination of bcc and fcc mechanisms of metals. *International Journal of Plasticity* 2005; **21**(8):1618–1639.
9. Jirasek M, Rolshoven S. Comparison of integral-type nonlocal plasticity models for strain-softening materials. *International Journal of Engineering Science* 2003; **41**(13/14):1553–1602.
10. Di Luzio G, Bazant ZP. Spectral analysis of localization in nonlocal and over-nonlocal materials with softening plasticity or damage. *International Journal of Solids and Structures* 2005; **42**(23):6071–6100.
11. Voyiadjis GZ, Dorgan RJ. Formulation of a gradient enhanced coupled damage-plasticity model. *American Society of Mechanical Engineers*, *Applied Mechanics Division*, *AMD* 2004; **255**:15–22.
12. Voyiadjis GZ, Al-Rub RKA. A physically based gradient plasticity theory. *International Journal of Plasticity* 2006; **22**(4):654–684.
13. Manzari MT, Regueiro RA. Gradient plasticity modelling of geomaterials in a meshfree environment. Part I: Theory and variational formulation. *Mechanics Research Communications* 2005; **32**(5):536–546.
14. de Borst R, Sluys LJ. Localisation in a Cosserat continuum under static and dynamic loading conditions. *Computer Methods in Applied Mechanics and Engineering* 1991; **90**:805–827.
15. Manzari MT. Application of micropolar plasticity to post failure analysis in geomechanics. *International Journal for Numerical and Analytical Methods in Geomechanics* 2004; **28**(10):1011–1032.
16. Ortiz M, Leroy Y, Needleman A. A finite element method for localized failure analysis. *Computer Methods in Applied Mechanics and Engineering* 1987; **61**(2):189–214.
17. Belytschko T, Fish J, Engelmann BE. A finite-element with embedded localization zones. *Computer Methods in Applied Mechanics and Engineering* 1988; **70**(1):59–89.
18. Garikipati K, Hughes TJR. A variational multiscale approach to strain localization—formulation for multidimensional problems. *Computer Methods in Applied Mechanics and Engineering* 2000; **188**(1–3):39–60.
19. Armero F. Large-scale modelling of localized dissipative mechanisms in a local continuum: applications to the numerical simulation of strain localization in rate-dependent inelastic solids. *Mechanics of Cohesive—Frictional Materials* 1999; **4**(2):101–131.
20. Simo JC, Armero F. Geometrically non-linear enhanced strain mixed methods and the method of incompatible modes. *International Journal for Numerical Methods in Engineering* 1992; **33**(7):1413–1449.
21. Simo JC, Oliver J, Armero F. An analysis of strong discontinuities induced by strain-softening in rate-independent inelastic solids. *Computational Mechanics* 1993; **12**:277–296.
22. Armero F, Garikipati K. An analysis of strong discontinuities in multiplicative finite strain plasticity and their relation with the numerical simulation of strain localization in solids. *International Journal of Solids and Structures* 1996; **33**(20/22):2863–2885.
23. Armero F, Callari C. Analysis of strong discontinuities in a saturated poro-plastic solid. *International Journal for Numerical Methods in Engineering* 1999; **46**(10):1673–1698.
24. Callari C, Armero F. Finite element methods for the analysis of strong discontinuities in coupled poro-plastic media. *Computer Methods in Applied Mechanics and Engineering* 2002; **191**(39/40):4371–4400.
25. Armero F, Park J. An analysis of strain localization in a shear layer under thermally coupled dynamic conditions. Part 2: Localized thermoplastic models. *International Journal for Numerical Methods in Engineering* 2003; **56**(14):2101–2133.

DOI: 10.1002/nme

26. Callari C, Armero F. Analysis and numerical simulation of strong discontinuities in finite strain poroplasticity. *Computer Methods in Applied Mechanics and Engineering* 2004; **193**(27/29):2941–2986.
27. Oliver J. Modelling strong discontinuities in solid mechanics via strain softening constitutive equations. 1. Fundamentals. *International Journal for Numerical Methods in Engineering* 1996; **39**(21):3575–3600.
28. Oliver J. Modelling strong discontinuities in solid mechanics via strain softening constitutive equations. 2. Numerical simulation. *International Journal for Numerical Methods in Engineering* 1996; **39**(21):3601–3623.
29. Oliver J, Huespe AE, Pulido MDG, Chaves E. From continuum mechanics to fracture mechanics: the strong discontinuity approach. *Engineering Fracture Mechanics* 2002; **69**(2):113–136.
30. Oliver J, Huespe AE, Samaniego E. A study on finite elements for capturing strong discontinuities. *International Journal for Numerical Methods in Engineering* 2003; **56**(14):2135–2161.
31. Oliver J, Huespe AE. Continuum approach to material failure in strong discontinuity settings. *Computer Methods in Applied Mechanics and Engineering* 2004; **193**(30–32):3195–3220.
32. Oliver J, Huespe AE, Samaniego E, Chaves EWV. Continuum approach to the numerical simulation of material failure in concrete. *International Journal for Numerical and Analytical Methods in Geomechanics* 2004; **28**(7–8): 609–632.
33. Regueiro RA, Borja RI. A finite element model of localized deformation in frictional materials taking a strong discontinuity approach. *Finite Elements in Analysis and Design* 1999; **33**(4):283–315.
34. Borja RI. A finite element model for strain localization analysis of strongly discontinuous fields based on standard Galerkin approximation. *Computer Methods in Applied Mechanics and Engineering* 2000; **190**(11/12):1529–1549.
35. Borja RI, Regueiro RA, Lai TY. FE modelling of strain localization in soft rock. *Journal of Geotechnical and Geoenvironmental Engineering* 2000; **126**(4):335–343.
36. Regueiro RA, Borja RI. Plane strain finite element analysis of pressure sensitive plasticity with strong discontinuity. *International Journal of Solids and Structures* 2001; **38**(21):3647–3672.
37. Borja RI, Regueiro RA. Strain localization in frictional materials exhibiting displacement jumps. *Computer Methods in Applied Mechanics and Engineering* 2001; **190**(20/21):2555–2580.
38. Borja RI. Finite element simulation of strain localization with large deformation: capturing strong discontinuity using a Petrov–Galerkin multiscale formulation. *Computer Methods in Applied Mechanics and Engineering* 2002; **191**(27/28):2949–2978.
39. Jirasek M. Comparative study on finite elements with embedded discontinuities. *Computer Methods in Applied Mechanics and Engineering* 2000; **188**(1/3):307–330.
40. Jirasek T, Zimmermann T. Embedded crack model. I. Basic formulation. *International Journal for Numerical Methods in Engineering* 2001; **50**(6):1269–1290.
41. Larsson R, Steinmann P, Runesson K. Finite element embedded localization band for finite strain plasticity based on a regularized strong discontinuity. *Mechanics of Cohesive—Frictional Materials* 1999; **4**(2):171–194.
42. Steinmann P. Finite element formulation for strong discontinuities in fluid-saturated porous media. *Mechanics of Cohesive—Frictional Materials* 1999; **4**(2):133–152.
43. Belytschko T, Moes N, Usui S, Parimi C. Arbitrary discontinuities in finite elements. *International Journal for Numerical Methods in Engineering* 2001; **50**(4):993–1013.
44. Stolarska M, Chopp DL, Moes N, Belytschko T. Modelling crack growth by level sets in the extended finite element method. *International Journal for Numerical Methods in Engineering* 2001; **51**(8):943–960.
45. Samaniego E, Belytschko T. Continuum-discontinuum modelling of shear bands. *International Journal for Numerical Methods in Engineering* 2005; **62**(13):1857–1872.
46. Wells GN, Sluys LJ. Analysis of slip planes in three-dimensional solids. *Computer Methods in Applied Mechanics and Engineering* 2001; **190**(28):3591–3606.
47. Wells GN, Sluys LJ. A new method for modelling cohesive cracks using finite elements. *International Journal for Numerical Methods in Engineering* 2001; **50**(12):2667–2682.
48. Mosler J, Meschke G. Embedded crack vs smeared crack models: a comparison of elementwise discontinuous crack path approaches with emphasis on mesh bias. *Computer Methods in Applied Mechanics and Engineering* 2004; **193**(30–32):3351–3375.
49. Oliver J, Cervera M, Manzoli O. Strong discontinuities and continuum plasticity models: the strong discontinuity approach. *International Journal of Plasticity* 1999; **15**(3):319–351.
50. Ruina A. Slip instability and state variable friction laws. *Journal of Geophysical Research* 1983; **88**(B12): 10359–10370.
51. Dieterich JH, Linker MF. Fault stability under conditions of variable normal stress. *Geophysical Research Letters* 1992; **19**(16):1691–1694.

DOI: 10.1002/nme

52. Rice JR, Ben-Zion Y. Slip complexity in earthquake fault models. *Proceedings of the National Academy of Sciences*, *U.S.A.* 1996; **93**:3811–3818.
53. Boulon MP, Garnica P, Vermeer PA. Soil–structure interaction: FEM computations. In *Mechanics of Geomaterial Interfaces*, Selvaduray APS, Boulon MJ (eds). Elsevier Science: Amsterdam, 1995; 147–171.
54. Simo JC, Rifai MS. Class of mixed assumed strain methods and the method of incompatible modes. *International Journal for Numerical Methods in Engineering* 1990; **29**(8):1595–1638.
55. Wong TF. Shear fracture energy of westerly granite from post-failure behavior. *Journal of Geophysical Research* 1982; **87**(NB2):990–1000.
56. Borja RI, Foster CD. Continuum mathematical modelling of slip weakening in geological systems. *Journal of Geophysical Research* 2007, in press.
57. Ben-Zion Y, Rice JR. Dynamic simulations of slip on a smooth fault in an elastic solid. *Journal of Geophysical Research* 1997; **102**(B8):17771–17784.
58. Linker MF, Dieterich JH. Effects of variable normal stress on rock friction: observations and constitutive equations. *Journal of Geophysical Research* 1992; **97**(B4):4923–4940.
59. Dieterich JH, Kilgore BD. Imaging surface contacts: power law contact distributions and contact stresses in quartz, calcite, glass and acrylic plastic. *Tectonophysics* 1996; **256**(1–4):219–239.
60. Mitchell JK. *Fundamentals of Soil Behavior* (2nd edn). Wiley: New York, NY, 1993.
61. Lapusta N, Rice JR, Ben-Zion Y, Zheng GT. Elastodynamic analysis for slow tectonic loading with spontaneous rupture episodes on faults with rate- and state-dependent friction. *Journal of Geophysical Research* 2000; **105**(B10):23765–23789.
62. Rice JR, Cocco M. Seismic fault rheology and earthquake dynamics. In *The Dynamics of Fault Zones*, *Dahlem Workshop Report 95*, Handy MR (ed.). The MIT Press: Cambridge, MA, 2006.
63. Johansson L, Klarbring A. Strong discontinuities and continuum plasticity models: the strong discontinuity approach. *Journal of Applied Mechanics* (ASME) 2000; **67**:267–273.
64. Christensen PW, Klarbring A, Pan JS, Stromberg N. Formulation and comparison of algorithms for frictional contact problems. *International Journal for Numerical Methods in Engineering* 1998; **42**(1):145–173.
65. Hughes TJR. *The Finite Element Method*. Prentice-Hall: Englewood Cliffs, NJ, 1987.
66. Wong TF. On the normal stress dependence of the shear fracture energy. In *Earthquake Source Mechanics*, Das S, Boatwright J, Scholz CH (eds). Geophysics Monograph, vol. 37. Maurice Ewing, vol. 6. American Geophysical Union: Washington, DC, 1986; 1–11.
67. Lapusta N. Modes of dynamic rupture propagation and rupture front speeds in earthquake models that account for dynamic weakening mechanisms. *EOS Transactions AGU* 2005; **86**(52):Abstract S34A-07.

DOI: 10.1002/nme